

### **3-D seismic velocity structure of the Kumaun-Garhwal (Central) Himalaya: Insight into the Main Himalayan Thrust and earthquake occurrence**

**Sandeep Gupta<sup>1,\*</sup>, P. Mahesh<sup>1,2</sup>, Nagaraju Kanna<sup>1</sup>, K. Sivaram<sup>1</sup>, Ajay Paul<sup>3</sup>**

<sup>1</sup>CSIR-National Geophysical Research Institute, Hyderabad - 500007, India

<sup>2</sup>CSIR-National Institute of Oceanography, Goa - 403004, India

<sup>3</sup>Wadia Institute of Himalayan Geology, Dehradun - 248001, India

\* Corresponding author: sandeepgupta@ngri.res.in; sandeep.ngri@gmail.com

#### **Summary**

Objective assessment of seismic hazard and understanding of the Himalayan arc's tectonics requires detailed information on the crustal structure and geometry of the underthrusting Indian Plate beneath the Himalaya. Here, we present high-resolution three-dimensional  $P$ - wave velocity ( $V_p$ ) and  $P$ -to- $S$  wave velocity ratio ( $V_p/V_s$ ) images of the Kumaun-Garhwal Himalaya, a proposed potential region for the future great earthquake. We generate these images by inverting arrival times of 515 local earthquakes recorded by 41 broadband stations during November 2006-June 2008. The tomographic images show a heterogeneous structure in the upper-mid crust. These images, along with available geophysical and geological information, indicate the presence of quartz-rich felsic rocks in the uppermost crust; and the occurrence of saline-rich aqueous fluid / partial melt in the upper-mid crust. We propose that the Main Himalayan Thrust (MHT), having a flat-ramp-flat geometry, lies at the base of these fluid zones. The small and moderate-to-strong magnitude earthquakes are mainly confined to the fluid-rich zones along the MHT and to quartz-rich rocks in the upper crust. Such an interpretation implies that the earthquake occurrence in the Kumaun-Garhwal Himalaya is largely controlled by the geometry of the MHT and crustal lithology.

**Key words:** Main Himalaya Thrust, brittle-ductile transition zone, mid-crustal ramp, fluids, seismic tomography, Central Himalaya

## 1. Introduction

The Himalayan mountain arc, one of the most spectacular subaerial mountain chains (Fig. 1a), was formed by the collision of the Indian Plate with the Eurasian Plate since ~50 million years (Patriat and Achache 1984). The Indian Plate continues to underthrust beneath southern Tibet at a speed of ~18-20 mm/year (Banerjee and Burgmann, 2002). This process has created several fault systems to the south of initial collision contact at the Indus-Tsangpo Suture Zone (ITSZ). These fault systems are marked by distinct litho-tectonic boundaries namely, from north to south, the Southern Tibetan Detachment (STD), Main Central Thrust (MCT), Main Boundary Thrust (MBT) and Main Frontal Thrust (MFT) (Fig. 1b) (Valdiya, 1980; Yin, 2006). At depth, the last three faults (MCT, MBT and MFT) are believed to sole into the top of the underthrusting Indian Plate beneath the Himalaya, which is commonly referred as the plane of detachment or the Main Himalayan Thrust (MHT, Fig. 1b Insert) (Zhao et al., 1993; Nelson, 1996). About half of the present-day convergence between the Indian and Eurasian Plates accommodates within the Himalaya and most of it through the stick and slip manner along the MHT (Zhao et al., 1993). This detachment plane was hypothesized on the basis of inferred rupture planes of great earthquakes and micro-seismicity (Seeber and Armbruster, 1981; Ni and Barazangi, 1984; Molnar, 1990). The up-dip and shallow part of the MHT below the Sub and Lower Himalaya is seismogenic, which accumulates strain during the inter-seismic period. On the other hand, the deeper and down-dip part of the MHT below the Higher and Tethys Himalaya slips aseismically. The large magnitude earthquakes in the Himalayan arc seem to rupture the seismogenic part of the MHT. On the other hand, small and moderate magnitude earthquakes occur on the down-dip part of the seismogenic MHT or on the mid-crustal ramp, which connects the gently dipping shallow up-dip seismically active part of the MHT and the aseismically slipping deeper down-dip part of the MHT (Seeber and Armbruster, 1981; Pandey et al., 1995; Lemonnier et al., 1999; DeCelles et al., 2001; Gahalaut, 2008). Various studies using seismic images, seismicity distribution and balanced cross-sections report variations in the geometry of the MHT, including the absence or presence of the mid-crustal ramp, and its location and dip along the Himalayan arc (Ni and Barazangi, 1984; Schelling and Arita, 1991; Srivastava and Mitra, 1994; Pandey et al., 1995; Schulte-Pelkum et al., 2005; C el erier et al., 2009; N ab elek et al., 2009; Hubbard et al., 2016; Elliott et al., 2016; Mendoza et al., 2019). As the seismic hazard due to high magnitude Himalayan earthquakes largely depends on the geometry of the MHT. Therefore, it is essential to understand the MHT in different Himalayan segments and its variation along the Himalayan arc.

The Kumaun-Garhwal Himalaya (77°-81°E), the area of the present investigation, is a part of ~700 km long central seismic gap between the ruptures of the 1905 Kangra (Ms 7.8) and the great 1934

Bihar (Mw 8.1) earthquakes (Fig. 1a) (Khattari, 1987; Bilham et al., 2001). This region has witnessed two significant historical earthquakes in the years 1505 and 1803 (Fig. 1a). The current seismicity (Mahesh et al., 2013) and geodetic measurements (Bilham et al., 2001) imply that this region is accumulating strain and the great earthquake is expected in the next few hundred years; both as gap-filling earthquakes in intervening regions and repeats of historical ruptures (Bilham and Ambraseys, 2005). No great or even major earthquake has occurred in past approximately two centuries within this seismic gap. The recent 2015 Gorkha earthquake (Mw 7.8) and damages caused by it have further highlighted the seismic hazard in the Kumaun-Garhwal Himalaya. Other than the background small magnitude micro-seismicity (Mahesh et al., 2013; Negi et al., 2017), this region has witnessed several moderate-to-strong earthquakes, namely, the 1991 Uttarkashi (Mw 6.8), 1999 Chamoli (Mw 6.5), 2005 Chamoli (Mb 5.3) and recent Rudraprayag (Mw 5.5 on 6 February 2017;  $M_b$  5.1 on 6 December 2017) earthquakes (Fig. 1b).

The balanced structural cross-sections (Srivastava and Mitra, 1994; C  l  rier et al., 2009), the 2-D seismic image using common conversion point (CCP) stacking of the *P-to-S* ( $P_s$ ) receiver functions (Caldwell et al., 2013), 2-D crustal shear velocity image using receiver functions modelling (Kanna and Gupta, 2020) and 2-D electrical resistivity image through inverting Magnetotelluric measurements (Rawat et al., 2014) report presence of the mid-crustal ramp on the MHT and a flat–ramp–flat geometry of the MHT in this region. However, unlike in the adjoining Nepal Himalaya, where the reported MHT geometry relates well with the seismic velocity images obtained using local seismic tomography (Monsalve et al., 2008), no study checks the correlation between the reported MHT geometry with the available seismic velocity images in the Kumaun-Garhwal Himalaya. Moreover, the seismic velocity images generated in this area are mostly confined to a small geological segment (Mukhopadhyay and Kayal, 2003; Mahesh et al., 2012, Kanaujia et al., 2016). Therefore, to fill this gap, we generate the  $V_p$  (*P*- wave velocity) and  $V_p/V_s$  (*P*-to-*S* wave velocity ratio) images using local earthquake tomography for the Kumaun-Garhwal Himalaya. We use these absolute  $V_p$  and  $V_p/V_s$  values to infer possible crustal compositions and possible nature of the MHT; and relate with the reported MHT geometry in this region. We also study the role of crustal composition and MHT geometry in earthquake generation in view of a potential threat of higher magnitude earthquake(s) in this particular part of the Himalaya.

## **2. Geology and Tectonics**

The Kumaun-Garhwal Himalaya lies between the Sutlej river in the west and the Kali river in the east. In the classic stratigraphic framework, it is divided into four physiographic subdivisions namely, from north to south, Tethyan Himalayas, Higher (or Great) Himalayas, Lower (or Lesser) Himalayas and Sub (or Outer) Himalayas extending southwards to the Himalayan foredeep, also called the

Gangetic plains/Ganga basin. These subdivisions are bounded to the south by a major north-dipping fault- the STD, MCT, MBT and MFT, respectively (Fig. 1). The MCT is bounded in the south by the Munsiri Thrust (MT or MCT1) and in the north by the Vaikrita Thrust (VT or MCT2). The Munsiri Thrust places the high-grade metamorphosed rocks of the Higher Himalayan Crystalline (HHC) over the Lower Himalayas rocks. These rocks are composed mainly of un-metamorphosed to low-grade metasediments and deformed by upper-crustal brittle thrusts. The Sub-Himalayas is comprising of the Neogene Siwalik formation. The major faults within the Lower Himalayas include the Tons Thrust (TT), Berinag thrust (BT), Ramgarh Thrust (RT), North Almora Thrust (NAT) and South Almora Thrust (SAT) (Fig. 1). Among these thrusts, the TT and NAT are south-dipping thrusts; on the other hand, the other thrusts are north dipping thrusts. Several authors have reviewed detailed geology and tectonics of the region (e.g., Valdiya, 1980; Srivastava and Mitra, 1994; Yin, 2006; C  lerier et al., 2009).

### **3. Data**

We use arrival time data from 515 well constrained local earthquakes of magnitude  $M > 1.0$  (yellow filled circles in Fig. 2, Supplementary Fig. S1) occurred during November 2006 - June 2008 and recorded at 41 seismic stations (blue and red filled circles in Fig. 1). Out of these 41 seismic stations, 31 stations (blue filled circles in Fig. 1) were operated by the CSIR-National Geophysical Research Institute (NGRI) and 10 stations (red filled circles in Fig. 1) were operated by the Wadia Institute of Himalayan Geology (WIHG). These stations were equipped with Guralp CMG-3 ESP/CMG-3T/Nanometrics Trillium T240 digital broadband seismometers and 24-bit data recorders (REFTEK RT 130-01/Nanometrics Taurus), with 4 GB swappable hard disk and Global Positioning System (GPS). The seismic waveforms were recorded continuously at the rate of 50 samples per second. Details about stations distribution and earthquake locations are provided in Mahesh et al. (2013). To ensure high-quality data set, we select only events which have registered a minimum of 5 *P*- and 3 *S*-arrivals. The uncertainties in arrival times picking of the first *P*- and *S*- arrival times are 0.05–0.2 and 0.1–0.3 s, respectively. After phase identification, we manually collect 7740 first *P*- and 6911 first *S*-arrival times from 515 selected earthquakes.

### **4. 3-D velocity tomography**

To decipher the crustal seismic structure of the Kumaun-Garhwal Himalaya, we invert 7740 first *P*- and 6911 first *S*- arrival times by using travel time inversion program SIMUL2000 (Thurber, 1983, 1997; Eberhart-Phillips, 1986). This program inverts *P*- arrival and *S*-*P* times of local earthquakes to obtain *P*-wave velocity, *P*-to-*S* wave velocity ratio ( $V_p/V_s$ ) and earthquake locations. In this study, we define the model space by 28–31.5°N, 77–81.0°E and 0–55 km in latitude, longitude and depth,

respectively, and with  $30.24^{\circ}\text{N}$ ,  $79.13^{\circ}\text{E}$  as the center of the model space. We parameterize the study region in terms of velocities at nodes of the 3-D grid and linear velocity gradients between the nodes. The velocity at any arbitrary point in the 3-D grid is calculated by linear interpolation between the surrounding nodes. We use flexible 3-D grid parameterization (Thurber and Eberhart-Phillips, 1999) with uneven spacing between grid nodes (Supplementary Fig. S2). We use an initial 1-D velocity model (Supplementary Fig. S3) and initial  $V_p/V_s$  (1.73) from Mahesh et al. (2013). The seismic ray paths distribution is shown in Fig. 2. We conduct several tomographic inversions with varying horizontal grid spacing (from 10 to 30 km) and vertical spacing (between 3 and 5 km). Though the patterns of tomographic images are mostly similar, there are small variations in the amplitude of velocity anomalies. We prefer the horizontal grid spacing of 15 km at the center of modelling space and 20-40 km for the rest of the model volume on each plane at 5, 10, 15, 20, 25 and 55 km depths. To suppress large perturbations in the calculated parameters, we use damping. The optimal damping parameters for the  $V_p$  and  $V_p/V_s$  are selected based on the empirical approach of Eberhart-Phillips (1986). To select the optimal value of damping factor, a trade-off curve between the data and model variances is constructed by performing several single step inversions with damping factor values ranging from 5 to 200 (Supplementary Fig. S4). After inversion, the variance reduction in the P- arrival time residuals and  $S$ - $P$  time are 60% and 54%, respectively. The average weighted root mean square residuals (RMS) for travel times decrease from 0.437 s to 0.238 s.

#### 4.1 Assessment of solution quality

In order to ascertain the adequacy of the ray coverage, spatial resolution and main features of the tomography images, we carry out various resolution tests and examine several parameters such as ray density (KHIT), Derivative Weighted Sum (DWS), Resolution Diagonal Element (RDE) and Spread Value (SV) of the resolution matrix (Toomey and Foulger, 1989; Evans et al., 1994; Michelini and McEvelly, 1991). The resolution tests of KHIT, DWS, RDE and SV for  $V_p$  and  $V_p/V_s$  are shown in Supplementary Figs. S5 and S6, respectively. Supplementary Fig. S7 compares the values of RDE and DWS for all the nodes of direct inversion for the finely gridded velocity model. The nodes with similar DWS or RDE have different spread values (SV), showing that neither of these two parameters can be used to evaluate the inversion quality. Therefore, we use these plots (Supplementary Fig. S7) to define a threshold SV, above which the results of the inversion will not be discussed as those corresponding to unresolved nodes. We empirically chose the threshold SV as 2 for  $V_p$  and  $V_p/V_s$ , because we observe that the regions with larger SV values show the smaller values of DWS and RDE (Supplementary Fig. S7).

We also carry out the Checkerboard Resolution Test (CRT). We assign positive and negative velocity perturbations ( $\pm 8\%$ ) at the alternate 3-D grid nodes in the modelling space to make a synthetic input model. Random errors in a normal distribution with a standard deviation of 0.1 s are also added to the theoretical travel times, which are calculated for the synthetic models. The test results show that the checkerboard images are recovered down to 25 km depth (Fig. 3).

Before describing the obtained results, to check the main features of the obtained images, we carry out two more tests namely, Restoring Resolution Test (RRT) and the synthetic test for the obtained tomographic images (Mukhopadhyay et al., 2006; Gupta et al., 2009a). In the RRT, we generate synthetic phase data by taking the obtained tomographic model as the input model and adding random errors having a normal distribution with a standard deviation of 0.1 s. We invert this synthetic data using other parameters (such as number of stations, events and inversion parameters) same as in the main inversion. The corresponding inversion results (Fig. 4) show that the  $V_p$  and  $V_p/V_s$  anomalies, as observed in main inversion, are well recovered. In the synthetic test, we generate synthetic phase data with respect to a synthetic model having a particular anomaly. We find significant variation in the  $V_p/V_s$  than in the  $V_p$  values in the obtained results. Therefore, we conduct this test for  $V_p/V_s$  anomaly along a cross-section across the study region. We make a synthetic model by using  $V_p/V_s$  values between 1.77 and 1.85 in the 6-30 km depth, and to the north of the RT. We use a fix  $V_p/V_s$  as 1.73 for remaining area (Fig. 5). After the inversion, following same procedure as applied on real data, we observe the higher values of the  $V_p/V_s$  are recovered with little smearing in the depth and horizontal directions (Fig. 5). Through these resolution tests, we believe that the main features of the tomographic result are reliably resolved by our data set and inversion.

## 5. Results

We show variations in absolute  $P$ - wave velocity ( $V_p$ ) and  $V_p/V_s$  ratio in plan view (Figs. 6 and S8). The micro seismicity within 2 km of either side of each depth layer is also projected on these images (Fig. 6). These seismic images show large-scale heterogeneity in the study region (Figs. 6 and S8). In general, up to 25 km depth, the absolute  $V_p$  and  $V_p/V_s$  vary between 4.8-6.8 km/s and 1.55-1.85, respectively. The images show that the smaller magnitude ( $M < 5$ ) earthquakes are generally concentrated in low  $V_p$  and low  $V_p/V_s$  zones at shallower depths ( $< 10$  km). On the other hand, the moderate-to-strong ( $5 < M < 7$ ) magnitude earthquakes are mostly concentrated in low  $V_p$  and high  $V_p/V_s$  zones at mid-crustal (12-20 km) depths.

To study the correlation between observed variations in  $V_p$  and  $V_p/V_s$  with the reported MHT geometry (Caldwell et al., 2013; Kanna and Gupta, 2020) and their linkage with the occurrence of

earthquakes in this region, we plot the  $V_p$  and  $V_p/V_s$  values along a cross-section (L1-L2 in Fig. 6). This cross-section passes through all the main Himalaya subdivisions and major faults in this area, and was earlier studied using receiver function analysis and modelling (Caldwell et al., 2013; Kanna and Gupta, 2020), Lg attenuation (Ashish et al., 2009) and magnetotelluric (Rawat et al., 2014) methods. Plotting of our results along this cross-section helps us integrate different results, to infer the possible rock composition and, thus, the nature of the upper-mid crust and the MHT. We also plot the moderate-to-strong magnitude earthquakes and the background seismicity, within 10 km either side of the cross-section, on the  $V_p$  and  $V_p/V_s$  images (Figs. 7a, b).

Based on the resolution tests (Figs. 4, 5 and S9), we discuss well-resolved features along this cross-section.

In general, the uppermost crust across the Kumaun-Garhwal Himalaya (up to ~7 km depth) is characterised by low  $V_p$  (~5.2-5.8 km/s) and low  $V_p/V_s$  (~1.53-1.65) (Figs. 7a, b). Similar values of  $V_p$  and  $V_p/V_s$  are observed in the uppermost crust of the Nepal Himalaya (Monsalve et al., 2008). In the sub-Himalayas, between the MFT and MBT, a 6 km thick zone (0-6 km depth) is characterized by low values of  $V_p$  (~5.2 - 5.4 km/s) and  $V_p/V_s$  (~1.65 - 1.70) (Figs. 7a, b). Further north in the Lower Himalayas and within 5 km depth, we observe two anomalous zones, marked as “J” and “K” (Figs. 7a, b). The zone “J” is characterised by normal values of  $V_p$  (~6.1 km/s) and  $V_p/V_s$  (~1.72). On the other hand, zone “K” appears with a higher value of  $V_p$  (~6.5 km/s) and moderate-to-high values of  $V_p/V_s$  (~1.72-1.78).

From 40 to 105 km north of the MFT and at 10-15 km depth, we observe a gently dipping layer with  $V_p$  (5.8-6.0 km/s) and  $V_p/V_s$  (~1.85) (zone “L”, Figs. 7a, b). From ~98 km north of the MFT and roughly beneath the surface location of the MT, this layer of low velocity and high  $V_p/V_s$  bends downward between 16 and 21 km depth with further reduction in  $V_p$  (5.2 km/s) and  $V_p/V_s$  (~1.82) (zone “M”, Figs. 7a, b). Further, 115 km north of the MFT onwards (zone “N”), this anomalous layer continues within same depth range (between 16 and 21 km) with relatively lower  $V_p$  (~6.0-6.2 km/s) and higher  $V_p/V_s$  (~1.78-1.82). This 4-6 km thick anomalous layer of lower  $V_p$  and higher  $V_p/V_s$  (L-M-N, Figs. 7a, b) well corroborates with earlier reported ~5 km thick layer with velocity reversal at similar depth (Fig. 7c) along the same cross-section (Caldwell et al., 2013; Kanna and Gupta, 2020).

## 6. Discussion

### 6.1 Crustal rock composition:

In the Kumaun-Garhwal Himalaya, which is a highly compressive region with confining pressure and elevated temperature (Shankar et al., 1999), the observed low  $V_p$  (~5.2-5.8 km/s) and low

$V_p/V_s$  (~1.53-1.65) in the uppermost crust (up to ~7 km depth) suggests the possible presence of quartz-rich felsic rocks (Kern, 1982; Sobolev and Babeyko, 1994; Christensen, 1996) throughout the Kumaun-Garhwal Himalaya. The widespread occurrence of such rocks (e.g., granite, gneisses, schists and quartzites) in the upper crust of this area also supports this interpretation. In the Lower Himalaya uppermost crust (0-6 km), the observed low  $V_p$  (~5.2-5.4 km/s), low  $V_p/V_s$  (~1.65-1.70) and low resistivity (~30 ohm-m, Rawat et al., 2014; Fig. 7d) suggest unconsolidated sediments above the basement. The basement is reported to be at ~6 km depth using geological (Srivastava and Mitra, 1994) and geophysical (Sarkar et al., 2008) studies. Further north in the Lower Himalaya, considering zones of high resistive (> 1000 ohm-m, Rawat et al., 2014, Fig. 7d), we interpret the two observed anomalous zones of higher  $V_p$  and higher  $V_p/V_s$  up to ~5 km depth (J and K, Fig. 7) as the possible signature of high-grade metamorphic rocks of the Lansdowne (zone “J”) and Almora (zone “K”) Klippes within low-grade metasedimentary rocks of the Lower Himalaya. These Klippes were transported from the region bounded between the VT and STD (Valdiya, 1980), however, due to poor resolution of our images in the north of the VT, we are unable to establish their source of origin as suggested by Valdiya (1980).

The Kumaun-Garhwal Himalaya is a high heat flow region (70-100 mW/m<sup>2</sup> near TPN station in Fig. 1, Shankar et al., 1999). In such a region, a 4-6 km thick anomalous layer of lower  $V_p$  and higher  $V_p/V_s$  in the mid-crust (L-M-N, Figs. 7a, b) may be due to occurrence of partial melt, aqueous fluids or both. Therefore, to constrain it we use other available information as well. This layer coincidences with an equally thick (~5 km) layer of shear-wave velocity reversal (Caldwell et al., 2013; Kanna and Gupta, 2020) and high conductivity (Rawat et al., 2014) (Figs. 7a-d). The MCT zone (“M”) and further north (“N”) are areas of lower  $V_p$  and higher  $V_p/V_s$  (Mahesh et al., 2012), high attenuation (low  $Q$  ~30–60, Ashish et al., 2009) and high conductance (>3000 S, Rawat et al., 2014; Fig. 7d). Further, a significant increase of  $V_p/V_s$  (from 1.6 to 1.82, Fig. 7b) at ~16 km depth indicates brittle-ductile zone around this depth, which is in good agreement with the cut-off depth (~16 km, Figs. 7a, b) of the observed micro-seismicity (Mahesh et al., 2013). A porous layer may even exist below a brittle-ductile transition (Marquis and Hyndman, 1992). Thus, by combining this information (high heat flow, high conductance, high attenuation, brittle-ductile transition depth and porous layer) with the observed lower  $V_p$  and higher  $V_p/V_s$  in the “M” and “N” zones, we infer the possible presence of partial melt with low melt fraction (Watanabe, 1993) in the porous layers within these zones (“M” and “N”). On the other hand, the normal  $V_p$  and higher  $V_p/V_s$  along with moderate conductance (1000 S, Rawat et al., 2014; Fig. 7d) and low attenuation (Ashish et al., 2009) in the zone “L” may be due to the saline-rich aqueous pore fluid.



The basement rocks of the underthrusting Indian crust are last seen to the south of the Gangetic plain before it underthrusts beneath the Himalaya. The upper crust is felsic (Jagadeesh and Rai, 2008; Kumar et al., 2012); the surface heat flow and radiogenic heat production are high (Kumar et al., 2009). As this high heat-producing felsic (with a lower melting point) upper crust along with sediments on its top underthrusts, due to shear heating the metamorphic dehydration of the underthrusting crust takes place. It induces water-saturated partial melting at lower temperatures in mid-crustal depth beneath the MCT zone (zone “M”, Figs. 7a, d). The high heat flow (70-100 mW/m<sup>2</sup>, Shankar et al., 1999) and the presence of tertiary granites in this region (Valdiya, 1980) also support the possibility of shallow partial-melting. Further, both (saline-rich aqueous fluid and partial melt) get separated and move independently. We argue that because of positive buoyancy, the saline-rich aqueous fluid moves in up-dip side of the underthrusting India crust (as seen in zone “L”, Figs. 7a-d). Moreover, as it moves upwards into the brittle portion of the crust, it alters the bulk chemical composition of the host rock and forms the quartz-rich felsic rocks (e.g., quartzite). On the other hand, the partial melt with low fluid fraction resides at the mid-crustal level to the north of the VT (zone “N”, Figs. 7a-d). We speculate that further north, the upward movement of this water-saturated melt along the STD (LeFort et al., 1987; Sachan et al., 2010) formed the Malari leucogranite (MaL in Figs. 1 and 7a-c), which is cut by the STD.

## 6.2 Configuration of the MHT

The MHT may be either at top or bottom of the intra-crustal low-velocity layer when formed due to subducting sediments or fluids, respectively (Zhang and Klemperer, 2010). In the Nepal Himalaya, the MHT has been identified at the positive velocity contrast (Schulte-Pelkum et al., 2005). We combine our inference of fluids (saline-rich aqueous fluids and partial melts) present in the mid-crust with the earlier information such as, positive velocity contrast (Caldwell et al., 2013; Kanna and Gupta, 2020), mid-crustal low shear velocity (Kanna and Gupta, 2020) and positive conductivity contrast (Rawat et al., 2014). We propose that the MHT is at the bottom of the observed low *P*-velocity and high *V<sub>p</sub>/V<sub>s</sub>* layer (continuous black line within dash lines showing uncertainties in Figs. 7a-d). We find that the observed flat-ramp-flat geometry of the MHT (Figs. 7a-d) corroborates very well with the earlier reported MHT in this area (Caldwell et al., 2013; Rawat et al., 2014; Kanna and Gupta, 2020).

The upper flat portion of the MHT dips gently up to 100 km from the MFT, roughly below the surface trace of the Munsiri Thrust (MT), and up to a depth of ~16 km. The ramp on the MHT is between 16 and 19 km depth and is ~10 km wide (between 100 and 110 km from the MFT). This gives ~17° dip of the ramp, which is in agreement with a 16° dip value as reported by Caldwell et al. (2013). The lower flat portion of the MHT starts at ~110 km distance from the MFT and a depth of ~19 km. It

continues further north with a very gentle dip. Using obtained MHT geometry and crustal composition, we observe that the change in rheology from brittle to ductile occurs at around upper flat-ramp junction of the MHT, which is roughly below the surface trace of the Muniary Thrust.

### 6.3 Linkage with the earthquake generation

To understand the roles of the crustal rocks composition and MHT geometry in the seismogenesis of the Kumaun-Garhwal Himalaya, we combine our observations of the fluids (saline-rich aqueous fluid and partial melts) and geometry of the MHT. The presence of fluids around and below a seismogenic zone can influence the activity of the fault system. It can affect the long-term structural and compositional evolution of the fault zone, and can alter the fault-zone strength and local stress regime (Sibson, 1992; Hickman et al., 1995; Gupta et al., 2009b; Mahesh et al., 2012). Therefore, due to enhanced fluids (partial melt and saline-rich aqueous fluid) content in the mid-crustal ramp zone (“M”, Fig. 7), this zone becomes weaker and represents a zone of extreme crustal deformation. This is evident by the occurrence of various moderate-to-strong magnitude earthquakes (e.g., 1999 Chamoli, 2005 Chamoli and 2017 Rudraprayag earthquakes) and smaller magnitude events in this zone (Figs. 1 and 7a, b). On the other hand, the occurrence of small magnitude earthquakes in the Lower Himalaya (zone “L”, Figs. 7a, b) are quite possibly related to increase in pore fluid pressure due to expelled saline-rich aqueous fluids along the MHT and weak bindings in minerals (like quartz) assemblage (Lowry and Gussinye, 2011) in the quartz-rich felsic rocks present in the upper crust. Moreover, steady aseismic deformation in the down-dip part of the MHT (north of the VT, zone “N” in Figs. 7a, b) is related to the occurrence of mid-crustal partial melt with a low fluid fraction (Cooper and Kohlstedt, 1986; Seeber and Armbruster, 1981; Nábelek et al., 2009).

A recent crustal deformation study using continuous GPS measurements suggests homogeneous and strong coupling (locking ratio  $> 0.5$ , seismically locked) on the MHT beneath the Sub and Lower Himalaya, and partial coupling (locking ratio  $< 0.4$ ) in the mid-crustal ramp on the MHT of this area (Yadav et al., 2019; Fig. 7e green line). The MHT is considered to be of locked rheology at temperature  $\leq 350^\circ\text{C}$  and of creeping rheology at temperature  $>450^\circ\text{C}$ . The zone between  $350^\circ\text{C}$  and  $450^\circ\text{C}$  isotherms is considered the transition zone between the locked and freely-creeping rheology of the MHT (Ader et al., 2012; Bilham et al., 2017).

The  $^{40}\text{Ar}/^{39}\text{Ar}$  thermochronology study in this area reports peak metamorphic temperatures  $\sim 370^\circ$  and  $480^\circ\text{C}$  to the north of the Tons Thrust (TT) and south of the Vaikrita Thrust (VT), respectively. The inverted thermal gradient varies between  $30^\circ$  and  $40^\circ\text{C}/\text{km}$  (Célérier et al., 2009). The suggested locked and creeping rheology zones by the GPS measurements (Yadav et al., 2019) relates with the

~370° and 480° C isotherms, respectively. Considering an average uniform thermal gradient of ~35° C/km; ~370° C to 480° temperature transition within 3.0 km (16 -19 km) depth and 17° dip of the MHT; the locked-creeping transition zone comes to be ~10 km wide ( $=3.0/\tan 17^\circ$ ). The location and width of the calculated locked-creeping transition zone well corroborate with the mid-crustal ramp on the MHT in the Kumaun-Garhwal Himalaya. Moreover, the micro-seismicity (zone “M”) and moderate-to-strong magnitude earthquakes also occur in this transition zone (Figs. 7a, b).

We link all the observations of the MHT geometry, locked-creeping transition zone, and brittle-ductile change in rheology along the MHT. We suspect that a zone at ~16-18 km below the surface trace of the Munsia Thrust in the Kumaun-Garhwal Himalaya (Fig. 7e) may be a nucleation zone for future higher magnitude earthquake(s), if any. However, it requires more multi-disciplinary studies using long term experiments in this region.

## 7. Conclusions

We generate images of the  $P$ - wave velocity ( $V_p$ ) and  $V_p/V_s$  ratio variations using local earthquake arrival time measurements recorded over 41 seismic stations operated during November 2006 to June 2008 in the Kumaun-Garhwal Himalaya, which is a proposed potential region for future great earthquake(s). In the 0-25 km depth, the  $V_p$  and  $V_p/V_s$  varies between 4.8-6.8 km/s and 1.55-1.85, respectively, and show a heterogeneous structure in the upper-mid crust. The seismic images exhibit signature of the unconsolidated sediments, close to the Main Frontal Thrust, and Klippes (Lansdowne and Almora) in the uppermost crust. In the upper-mid crust, the observed low  $V_p$  and high  $V_p/V_s$  (1.82-1.85) along with available conductivity values indicate the occurrence of saline-rich aqueous fluid and partial melt. Using the inferred crustal composition and constraints from earlier information, we propose the bottom of these fluid zones as the top of the underthrusting India Plate, which shows a flat-ramp-flat geometry at 16-21 km depth. The earthquakes of moderate and smaller magnitude mostly occur in the fluid-rich zone above the mid-crustal ramp in the underthrusting Indian Plate. The smaller magnitude earthquakes also occur in the quartz-rich upper crust. On the other hand, the steady aseismic deformation along the deeper flat portion of the underthrusting Indian Plate is due to partial melt with a low fluid fraction. The inferred rheology of the region is consistent with the seismic behavior of the MHT and provide constraints on the earthquake genesis in the Kumaun-Garhwal Himalaya.

**Acknowledgements:** We are very thankful to other members of the seismological field teams for helping in setting up seismological stations and data acquisition. The broadband seismic stations operated by Council of Scientific and Industrial Research-National Geophysical Research Institute (CSIR-NGRI) were supported by the Department of Science and Technology, Government of India.

We acknowledge critical discussions with Prof. Shyam S. Rai, Dr. V. K. Gahalaut and Prof. Nikolai Shapiro. All the authors thank their respective institutes for the necessary support. We are very much grateful to the editor Prof. Gabi Laske and two reviewers for their very exhaustive review and providing critical comments to improve the quality of the manuscript significantly.

## References:

- Ader, T., Avouac, J.-P., Liu Zeng, J., Lyon-Caen, H., Bollinger, L., Galetzka, J., Genrich, J., Thomas, M., Chanard, K., Sapkota, S.N., Rajur, S., Shrestha, P., Ding, L. & Flouzat, M., 2012. Convergence rate across the Nepal Himalaya and interseismic decoupling on the main Himalayan thrust: implications for seismic hazard, *J. Geophys. Res.*, **117**, B044403. <http://dx.doi.org/10.1029/2011JB009071>.
- Ashish, Padhy, A., Rai, S.S. & Gupta, S., 2009. Seismological evidence for shallow crustal melt beneath the Garhwal High Himalaya, India: implications for Himalayan channel flow, *Geophys. J. Int.*, **177** (1), 1111-1120.
- Banerjee, P. & Burgmann, R., 2002. Convergence across the northwest Himalaya from GPS measurements. *Geophys. Res. Lett.*, **29** (13), 30–34.
- Bilham, R., Gaur, V.K. & Molnar, P., 2001. Himalayan Seismic Hazard, *Science*, **293**, 1442-1442.
- Bilham, R. & Ambraseys, N., 2005. Apparent Himalayan slip deficit from the summation of seismic moments for Himalayan earthquakes 1500–2000, *Curr. Sci.*, **88**, 1658–1663.
- Bilham, R., Mencin, D., Bendick, R. & Bürgmann, R., 2017. Implications for elastic energy storage in the Himalaya from the Gorkha 2015 earthquake and other incomplete ruptures of the Main Himalayan Thrust, *Quaternary International*, **462**, 3-21.
- Caldwell, W.B., Klemperer, S.L., Lawrence, J.F., Rai, S.S. & Ashish, 2013. Characterizing the Main Himalayan Thrust in the Garhwal Himalaya, India with receiver function CCP stacking, *Earth and Planet. Sci. Lett.*, **367**, 15–27.
- Célérier, J., Harrison, T.M., Webb, A.A.G. & Yin, A., 2009. The Kumaun and Garhwal Lesser Himalaya, India. Part 1: Structure and stratigraphy, *Geol. Soc. Am. Bull.*, **121** (9-10), 1262–1280, doi: 10.1130/B26344.1.
- Christensen, N.I., 1996. Poisson's ratio and crustal seismology, *J. Geophys. Res.*, **101**, 3139–3156.
- Cooper, R.F. & Kohlstedt, D.L., 1986. Rheology and structure of olivine-basalt partial melts, *J. Geophys. Res.*, **91** (B9), 9315-9323, doi.org/10.1029/JB091iB09p09315.
- DeCelles, P.G., Robinson, D.M., Quade, J., Ojha, T.P., Garzzone, C.N., Copeland, P. & Upreti, B.N., 2001. Stratigraphy, structure, and tectonic evolution of the Himalayan fold-thrust belt in western Nepal, *Tectonics*, **20** (4), 487–509.
- Eberhart-Phillips, D., 1986. Three-dimensional velocity structure in northern California coast ranges from inversion of local earthquakes, *Bull. Seism. Soc. Am.*, **76**, 1025–1052.
- Elliott, J.R., Jolivet, R., Gonzalez, P.J., Avouac, J.-P., Hollingsworth, J., Searle, M.P. & Stevens, V.L., 2016. Himalayan megathrust geometry and relation to topography revealed by the Gorkha earthquake, *Nat. Geosci.*, **9**, 174-180.
- Evans, J.R., Eberhart-Phillips, D. & Thurber, C.H., 1994. User's manual for SIMULPS12 for imaging Vp and Vp/Vs: a derivative of the “Thurber” tomographic inversion SIMUL3 for local earthquakes and explosions, Open-file Report 94–431. U.S. Geological Survey 101 pp.
- Gahalaut, V.K., 2008. Major and great earthquakes and seismic gaps in the Himalayan arc, *Geol. Soc. of India, Memoir* **66**, 373-393.
- Gupta, S., Zhao, D. & Rai, S.S., 2009a. Seismic imaging of the mantle under the Erebus hotspot in Antarctica, *Gondwana Res.*, **16**, 109-118.

- Gupta, S., Zhao, D., Ikeda, M., Ueki, S. & Rai, S.S., 2009b. Crustal tomography under the Median Tectonic Line in Southwest Japan using P and PmP data, *J. Asian Earth Sciences*, **35**, 377-390.
- Hickman, S., Sibson, R. & Bruhn, R., 1995. Introduction to special section: mechanical involvement of fluids in faulting, *J. Geophys. Res.*, **100**, 12831-12840.
- Hubbard, J., Almeida, R., Foster, A., Sapkota, S.N., Burgi, P. & Tapponnier, P., 2016. Structural segmentation controlled the 2015 M<sub>w</sub> 7.8 Gorkha earthquake rupture in Nepal, *Geology*, **44(8)**, 639-642.
- Jagadeesh, S. & Rai, S.S., 2008. Thickness, composition, and evolution of the Indian Precambrian crust inferred from broadband seismological measurements, *Precam. Res.*, **162**, 4-15.
- Kanaujia, J., Kumar, A. & Gupta, S.C., 2016. 3-D velocity structure around tehri region of the Garhwal lesser Himalaya: constraints on geometry of the underthrusting Indian plate, *Geophys J. Int.*, doi: 10.1093/gji/ggw056.
- Kanna, N. & Gupta, S., 2020. Crustal seismic structure beneath the Garhwal Himalaya using regional and teleseismic waveform modelling, *Geophys J. Int.*, **222(3)**, 2040-2052, doi.: 10.1093/gji/ggaa282.
- Kern, H., 1982. P- and S- wave velocities in crustal and mantle rocks under the simultaneous action of high confining pressure and high temperature and the effect of the rock microstructure, In *High-Pressure Researches in Geosciences*, pp. 15-45, ed, Schreyer, W., E. Schweizerbart'sche Verlagsbuchhandlung, Stuttgart.
- Khattri, K.N., 1987. Great earthquakes, seismicity gaps and potential for earthquake disaster along the Himalaya plate boundary, *Tectonophys.*, **138**, 79-92.
- Kumar, P.S., Menon, R. & Reddy, G., 2009. Heat production heterogeneity of the Indian crust beneath the Himalaya: insights from the northern Indian shield, *Earth Planet. Sci. Lett.*, **283 (1-4)**, 190-196.
- Kumar, T.V., Jagadeesh, S. & Rai, S.S., 2012. Crustal structure beneath the Archaean- Proterozoic terrain of north India from receiver function modelling, *J. Asian Earth Sci.*, **58**, 108-118.
- LeFort, P., Cuney, M., Deniel, C., France-Lanord, C., Sheppard, S.M. F., Upreti, B.N. & Vidal, P., 1987. Crustal generation of the Himalayan leucogranites, *Tectonophys.*, **134**, 39-57, doi: 10.1016/0040-1951(87)90248-4.
- Lemonnier, C., Marquis, G., Perrier, F., Avouac, J.P., Chitrakar, G., Kafle, B., Sapkota, S., Gautam, U., Tiwari, D. & Bano, M., 1999. Electrical structure of the Himalaya of central Nepal: high conductivity around the mid-crustal ramp along the MHT, *Geophys. Res. Lett.*, **26 (21)**, 3261-3264.
- Lowry, A.R. & Gussinye, M.P., 2011. The role of crustal quartz in controlling Cordilleran deformation, *Nature*, **471**, 353-357, doi:10.1038/nature09912.
- Mahesh, P., Gupta, S., Rai, S.S. & Sarma, P.R., 2012. Fluid driven earthquakes in the Chamoli region, Garhwal Himalaya: Evidence from local earthquake tomography, *Geophys. J. Int.*, **191 (3)**, 1295-1304, doi: 10.1111/j.1365-246X.2012.05672.x.
- Mahesh, P., Rai, S.S., Sivaram, K., Paul, A., Gupta, S., Sarma, P.R. & Gaur, V.K., 2013. One dimensional reference velocity model and precise locations of earthquake hypocenters in the Kumaon- Garhwal Himalaya, *Bull. Seismol. Soc. Am.*, **103 (1)**, 328-339.
- Marquis, G. & Hyndman, R.D., 1992. Geophysical support for aqueous fluids in the deep crust: seismic and electrical relationships, *Geophys. J. Int.*, **110 (1)**, 91-105, <https://doi.org/10.1111/j.1365-246X.1992.tb00716.x>.
- Mendoza, M.M., Ghosh, A., Karplus, M.S., Klemperer, S.L., Sapkota, S.N., Adikari, L.B. & Velsco, A., 2019. Duplex in the Main Himalaya Thrust illuminated by aftershocks of the 2015 M<sub>w</sub> Gorkha earthquake, *Nature*, **12**, 1018-1022.

- Michellini, A. & McEvelly, T.V., 1991. Seismological studies at Parkfield: I. Simultaneous inversion for velocity structure and hypocenters using cubic B-splines parameterization, *Bull. Seismol. Soc. Am.*, **81**, 524–552.
- Molnar, P., 1990. A review of the seismicity and the rates of active thrusting and deformation at the Himalaya, *J. Himalayan Geol.*, **1**, 131-154.
- Monsalve, G., Sheehan, A., Rowe, C. & Rajaure, S., 2008. Seismic structure of the crust and the upper mantle beneath the Himalayas: Evidence for eclogitization of lower crustal rocks in the Indian Plate, *J. Geophys. Res.*, **113**, B08315, doi:10.1029/2007JB005424.
- Mukhopadhyay, S. & Kayal, J.R., 2003. Seismic Tomography structure of the 1999 Chamoli Earthquake source area in the Garhwal Himalaya, *Bull. Seismol. Soc. Am.*, **93**, 1854–1861.
- Mukhopadhyay, S., Mishra, O.P., Zhao, D., Kayal, J.R., 2006. 3-D seismic structure of the source area of the 1993 Latur, India, earthquake and its implications for rupture nucleations, *Tectonophys.*, **415**, 1–16.
- Nábelek, J., et al., 2009. Underplating in the Himalaya-Tibet collision zone revealed by the Hi-CLIMB experiment, *Science*, **325(5946)**, 1371–1374.
- Negi, S.S., Paul, A., Cesca, S., Kamal, Kriegerowski, M., Mahesh, P. & Gupta, S., 2017. Crustal velocity structure and earthquake processes of Garhwal-Kumaun Himalaya: Constraints from Regional Waveform Inversion and Array Beam Modelling, *Tectonophys.*, **712-713**, 45-63, doi:10.1016/j.tecto.2017.05.007.
- Nelson, K., 1996. Partially molten middle crust beneath southern Tibet: Synthesis of project INDEPTH results, *Science*, **274**, 1684–1688.
- Ni, J., Barazangi, M., 1984. Seismotectonics of the Himalayan collision zone: Geometry of the underthrusting Indian plate beneath the Himalaya, *J. Geophys. Res.*, **89**, 1147-1163.
- Pandey, M.R., Tandukar, R.P., Avouac, J.P., Lave, J. & Massot, J.P., 1995. Interseismic strain accumulation on the Himalayan crustal ramp (Nepal), *Geophys. Res. Lett.*, **22 (7)**, 751–754.
- Patriat, P. & Achache, J., 1984. India–Asia collision chronology has implications for crustal shortening and diving mechanism of plates, *Nature*, **311**, 615–621.
- Rawat, G., Arora, B.R. & Gupta, P.K., 2014. Electrical resistivity cross-section across the Garhwal Himalaya: proxy to fluid-seismicity linkage, *Tectonophys.*, **637**, 68–79.
- Sachan, H.K., Kohn, M.J., Saxena, A. & Corrie, S.L., 2010. The Malari leucogranite, Garhwal Himalaya, northern India: Chemistry, age, and tectonic implications, *Geol. Soc. Am. Bull.*, **122**, 1865-1876, doi: 10.1130/B30153.1.
- Sarkar R.K., Saha, D.K. & Chowdhuri, S.N., 2008. Identification and Mapping of the Intracrustal Density Interfaces of a part of Kumaun-Garhwal Himalaya from Harmonic Inversion of Bouguer Anomaly, *Himalayan Geology*, **29 (1)**, 81-85.
- Schelling, D. & Arita, K., 1991. Thrust tectonics, crustal shortening, and the structure of the far-eastern Nepal Himalaya, *Tectonics*, **10 (5)**, 851–862, URL <http://dx.doi.org/10.1029/91TC01011>.
- Schulte-Pelkum, V., Monsalve, G., Sheehan, A., Pandey, M.R., Sapkota, S., Bilham, R. & Wu, F., 2005. Imaging the Indian subcontinent beneath the Himalaya, *Nature*, **435**, 1222–1225.
- Seeber, L. & Armbuster, J.G., 1981. Great detachment earthquakes along the Himalayan arc and long-term forecasts. In: D.W Simpson and P.G. Richards (Editors), Earthquake Prediction, An International Review, Maurice Ewing series 4., *Am. Geophys. Union*, Washington, DC, pp. 259-279.
- Shankar, R., Absar & A., Bajpai, I.P., 1999, Heat flow map of India – an update, In: Simmons S.F., Morgan, O.E., Dunstall, M.G. (Eds.) Proc. 21<sup>st</sup> New Zealand Geothermal workshop, Nov. 10-12, 1999, University of Auckland, Auckland, New Zealand. 157-162.
- Sibson, R.H., 1992. Implications of fault-value behavior for rupture nucleation and recurrence, *Tectonophys.*, **11**, 283-293.

- Sobolev, S.V. & Babeyko, A.Y., 1994. Modeling of mineralogical composition, density and elastic wave velocities in the anhydrous rocks, *Surveys in Geophysics*, **15**, 515-544, doi: 10.1007/BF00690173.
- Srivastava, P. & Mitra, G., 1994. Thrust geometries and deep structure of the outer and lesser Himalaya, Kumaun and Garhwal (India): Implication for evolution of the Himalaya fold-and-thrust belt, *Tectonics*, **13** (1), 89–109, doi: 10.1029/93TC01130.
- Thurber, C.H., 1983. Earthquake locations and three dimensional crustal velocity structure in the Coyote lake area, central California, *J. Geophys. Res.*, **88**, 8226–8236.
- Thurber, C., Roecker, S., Ellsworth, W., Chen, Y., Lutter, W. & Sessions, R., 1997. Two-dimensional seismic image of the San Andreas fault in the Northern Gabilan Range, central California: evidence for fluids in the fault zone, *Geophys. Res. Lett.*, **24**, 1591–1594.
- Thurber, C.H. & Eberhart-Phillips, D., 1999. Local earthquake tomography with flexible gridding, *Computers & Geosci.*, **25**, 809-818.
- Toomey, D.R. & Foulger, G.R., 1989. Tomographic inversion of local earthquake data from the Hengill-Grensdalur central volcano complex, Iceland, *J. Geophys. Res.*, **94**, 17,497–17,510.
- Valdiya, K.S., 1980. Geology of the Kumaon Lesser Himalaya, *Wadia Institute of Himalaya*, Dehra Dun, India, 291 pp.
- Watanabe, T., 1993. Effects of water and melt on seismic velocities and their application to characterization of seismic reflectors, *Geophys. Res. Lett.*, **20** (24), 2933-2936.
- Yadav, R.K., Gahalaut, V.K., Bansal, A.K., Sati, S.P., Catherine, J., Gautam, P., Kumar, K. & Rana, N., 2019. Strong seismic coupling underneath Garhwal–Kumaun region, NW Himalaya, India, *Earth and Planet. Sci. Lett.*, **506**, 8-14.
- Yin, A., 2006. Cenozoic tectonic evolution of the Himalayan orogen as constrain by along strike variation of structural geometry, exhumation history and foreland sedimentation, *Earth Sci. Rev.*, **76**, 1-132.
- Zhang, Z. & Klempnerer, S., 2010. Crustal structure of the Tethyan Himalaya, southern Tibet: new constraints from old wide-angle seismic data, *Geophys. J. Int.*, **181** (3), 1247–1260, URL <http://dx.doi.org/10.1111/j.1365-246X.2010.04578.x>.
- Zhao, W., Nelson, K.D. & Project INDEPTH Team., 1993. Deep seismic reflection evidence for continental underthrusting beneath southern Tibet, *Nature*, **366**, 557–559.

## List of Figures

- Figure 1:** (a) Topography map of the Himalayan region showing rupture zones (orange shaded) of significant historical earthquakes, central seismic gap (blue ellipse) and study region (yellow rectangular box). (b) Tectonic map of study area showing subdivisions of Kumaun-Garhwal Himalaya by major thrusts (continuous lines) viz., MFT: Main Frontal Thrust, MBT: Main Boundary Thrust, TT: Tons Thrust, RT: Ramgarh Thrust, SAT: South Almora Thrust, NAT: North Almora Thrust, MT: Munsiri Thrust, VT: Vaikrata Thrust, STD: Southern Tibetan Detachment (modified after Valdiya, 1980; Yin, 2006). The seismic stations used in the study are shown as small filled circles. Moderate-to-strong magnitude earthquakes in the region are shown as stars (Magenta: 1991 Uttarkashi, M 6.6; Green: 1999 Chamoli, M 6.3; Light blue: 2005 Chamoli, M 5.3; Blue: February 2017 Rudraprayag, M 5.8; Red: December 2017 Rudraprayag, M 5.5). Small ellipse shows the location of the Malari Leucogranites (MaL). (Inset left bottom) The simplified tectonic model of the Himalaya Orogen.
- Figure 2:** 3-D distribution of seismic ray paths. The seismic stations and events are shown by red triangles and yellow dots, respectively. Major tectonic boundaries (as shown in Fig. 1b) are also projected with blue lines.
- Figure 3:** Results of the checkerboard resolution tests (CRT) for  $V_p$  (a), and  $V_p/V_s$  (b). Layer depth is shown on the lower-left corner of each map. Scales for perturbation values (in %) for both  $V_p$  and  $V_p/V_s$  are shown in the right.
- Figure 4:** Results of restoring resolution test along a L1-L2 (as shown in Fig. 6). Panels (a) and (b) show the original and restored models for  $V_p$ , respectively. Panels (c) and (d) show the original and restored models for  $V_p/V_s$ , respectively. Kindly refer the text (section 4.1) for detail.
- Figure 5:** Results of synthetic test along a L1-L2 (as shown in Fig. 6). Panels (a) and (b) show the original and restored models for  $V_p/V_s$ , respectively. Kindly refer the text (section 4.1) for detail.
- Figure 6:** Plan view of tomographic images of absolute  $P$ -wave velocity ( $V_p$ ) (a) and  $V_p/V_s$  (b). Layer depth is shown on the upper-left corner of each map. The  $V_p$  and  $V_p/V_s$  scales are shown at the bottom of respective plots. Poorly resolved areas are masked by gray colour in each plot. Small open circles indicate the small magnitude earthquakes during 2006-2008, which occurred within 2 km of each depth slice. Earthquake magnitude scale is shown in lower-left plot of Fig. 6a. Moderate-to-strong magnitude ( $5.0 < M < 7.0$ ) earthquakes in the region are shown with different stars, same as mentioned in Fig. 1. Tectonic boundaries are same as shown in Fig. 1b. L1 - L2 shows the location of cross-section, used for showing  $V_p$  and  $V_p/V_s$  images to correlate with the MHT across the Kumaun-Garhwal Himalaya in Fig. 7.
- Figure 7:** (a, b) Vertical cross-sections of the  $P$ - wave velocity ( $V_p$ ) and  $V_p/V_s$  images along the profile L1-L2 (as shown in Fig. 6). Small open circles show small magnitude earthquakes that occurred within 50 km width on either side of the profile and recorded during 2006-2008. Moderate-to-strong magnitude ( $5.0 < M < 7.0$ ) earthquakes in the region are shown with different stars, same as mentioned in Fig. 1. The inferred MHT (continuous black line) along with uncertainty (dotted line with white slanting lines) are projected over these images. MaL represents the Malari Leucogranites. Please see text for details of the inferred features (“J”, “K”, “L”, “M”, “N”, “MaL” and MHT). Topography variation along the profile is shown on the top. (c) Inferred MHT and 1-D shear wave velocity models using receiver function modelling (Kanna and Gupta, 2020) superimposed over obtained  $V_p/V_s$  images. (d) Inferred MHT superimposed over resistivity values (Rawat et al., 2014). (e) Schematic diagram showing the nature and geometry of the MHT (gray colour with dash lines) in the Garhwal



Himalaya and its role in earthquake genesis, by combining observation from seismology, magnetotellurics and GPS. Green line shows the seismic coupling derived from the slip deficit rate (Yadav et al., 2018). Its scale is shown on the right axis. H/V is 1:1 for the Figs. 7 (a-d).

### Supplementary Figures

- Fig. S1:** 3-D distribution of the 515 earthquakes (open circles) used in the study. The size and colour of open circles represents the earthquake magnitude as per inset in the top-left corner of the plot. The earthquake magnitude histogram is shown in lower-right side of the plot. Depth scale is exaggerated.
- Fig. S2:** Grid point distribution in the plan view. The same grid points were taken at different depths (5, 10, 15, 20, 25 and 55 km).
- Fig. S3:** Initial 1-D velocity model (Mahesh et al., 2013) used for the tomography.
- Fig. S4:** Trade-off curves between data variance and model variance for  $V_p$  (a) and  $V_p/V_s$  (b), used to select the optimal damping parameters to obtain the optimum 3-D  $V_p$  and  $V_p/V_s$  images.
- Fig. S5:** (a) Total number of hit per cell (KHIT), (b) Derivative Weighted Sum (DWS), (c) Resolution Diagonal Element (RDE), and (d) Spread Value (SV) of resolution matrix for  $V_p$  at different depths. Layer depth is shown on the lower-left corner of each map. Tectonic boundaries are same as shown in Fig. 1.
- Fig. S6:** (a) Total number of hit per cell (KHIT), (b) Derivative Weighted Sum (DWS), (c) Resolution Diagonal Element (RDE), and (d) Spread Value (SV) of resolution matrix for  $V_p/V_s$  at different depths. Layer depth is shown on the lower-left corner of each map. Tectonic boundaries are same as shown in Fig. 1.
- Fig. S7:** Derivative Weighted Sum (DWS) versus Spread Values (SV) for  $V_p$  (a) and  $V_p/V_s$  (b). Resolution Diagonal Element (RDE) value versus Spread Values for  $V_p$  (c) and  $V_p/V_s$  (d). The arrows indicate the threshold values of the Spread Value chosen to delineate poorly resolved in subsequent velocity maps.
- Fig. S8:** Plan view of tomographic images of absolute  $P$ -wave velocity ( $V_p$ ) (a) and  $V_p/V_s$  (b), same as Fig. 6, however without earthquakes.
- Fig. S9:** Total number of Hit (KHIT), Derivative Weighted Sum (DWS), Resolution Diagonal Element, and Spread Value (SV) of resolution matrix for  $V_p$  (a, b, c, d) and for  $V_p/V_s$  (e, f, g, h) along the profile L1-L2 (as shown in Fig. 6).

## Figures

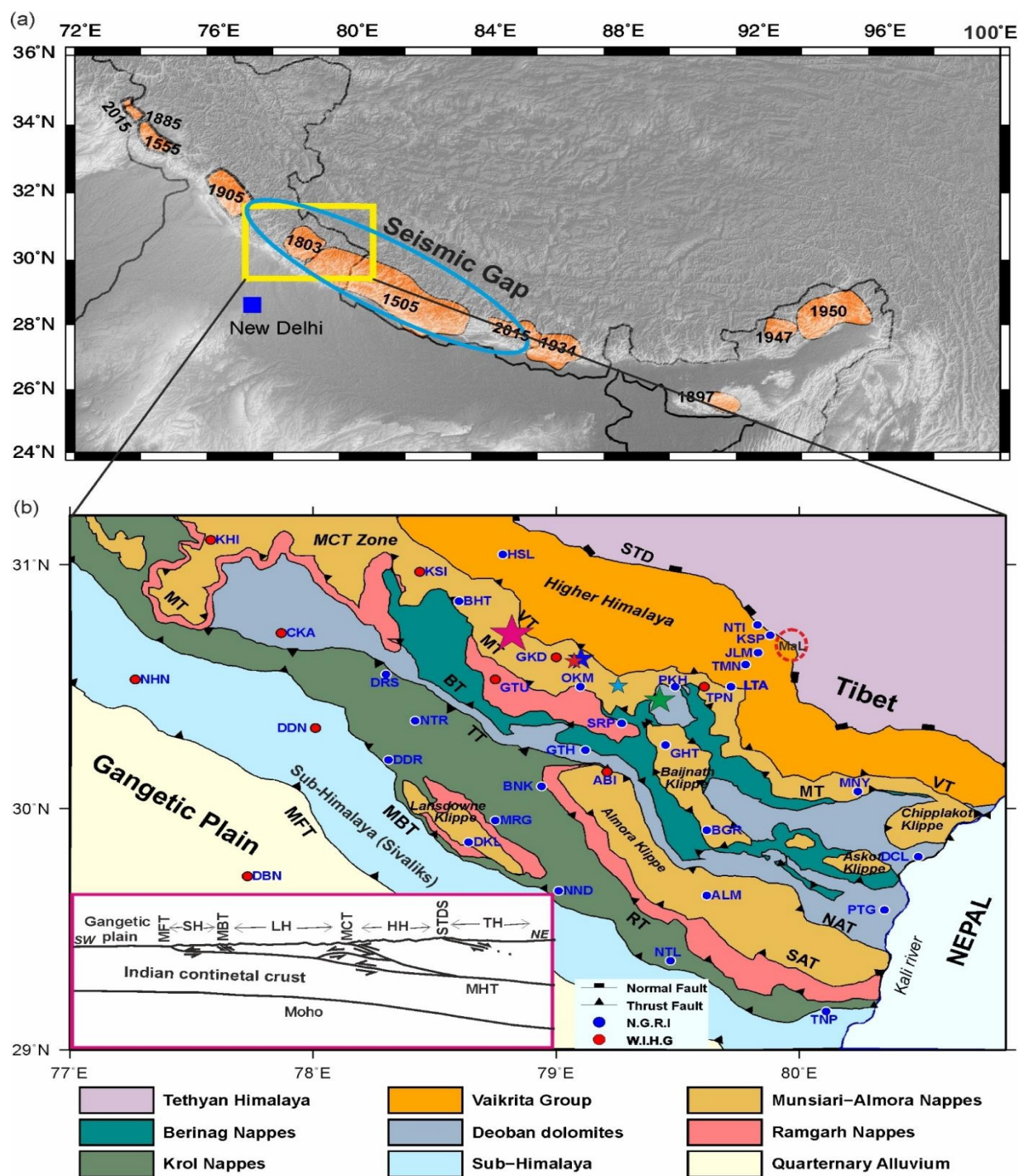


**Figure 1:** (a) Topography map of the Himalayan region showing rupture zones (orange shaded) of significant historical earthquakes, central seismic gap (blue ellipse) and study region (yellow rectangular box). (b) Tectonic map of study area showing subdivisions of Kumaun-Garhwal Himalaya by major thrusts (continuous lines) viz., MFT: Main Frontal Thrust, MBT: Main Boundary Thrust, TT: Tons Thrust, RT: Ramgarh Thrust, SAT: South Almora Thrust, NAT: North Almora Thrust, MT: Munsiri Thrust, VT: Vaikrata Thrust, STD: Southern Tibetan Detachment (modified after Valdiya, 1980; Yin, 2006). The seismic stations used in the study are shown as small filled circles. Moderate-to-strong magnitude earthquakes in the region are shown as stars (Magenta: 1991 Uttarkashi, M 6.6; Green: 1999 Chamoli, M 6.3; Light blue: 2005 Chamoli, M 5.3; Blue: February 2017 Rudraprayag, M 5.8; Red: December 2017 Rudraprayag, M 5.5). Small ellipse shows the location of the Malari Leucogranites (MaL). (Inset left bottom) The simplified tectonic model of the Himalaya Orogen.

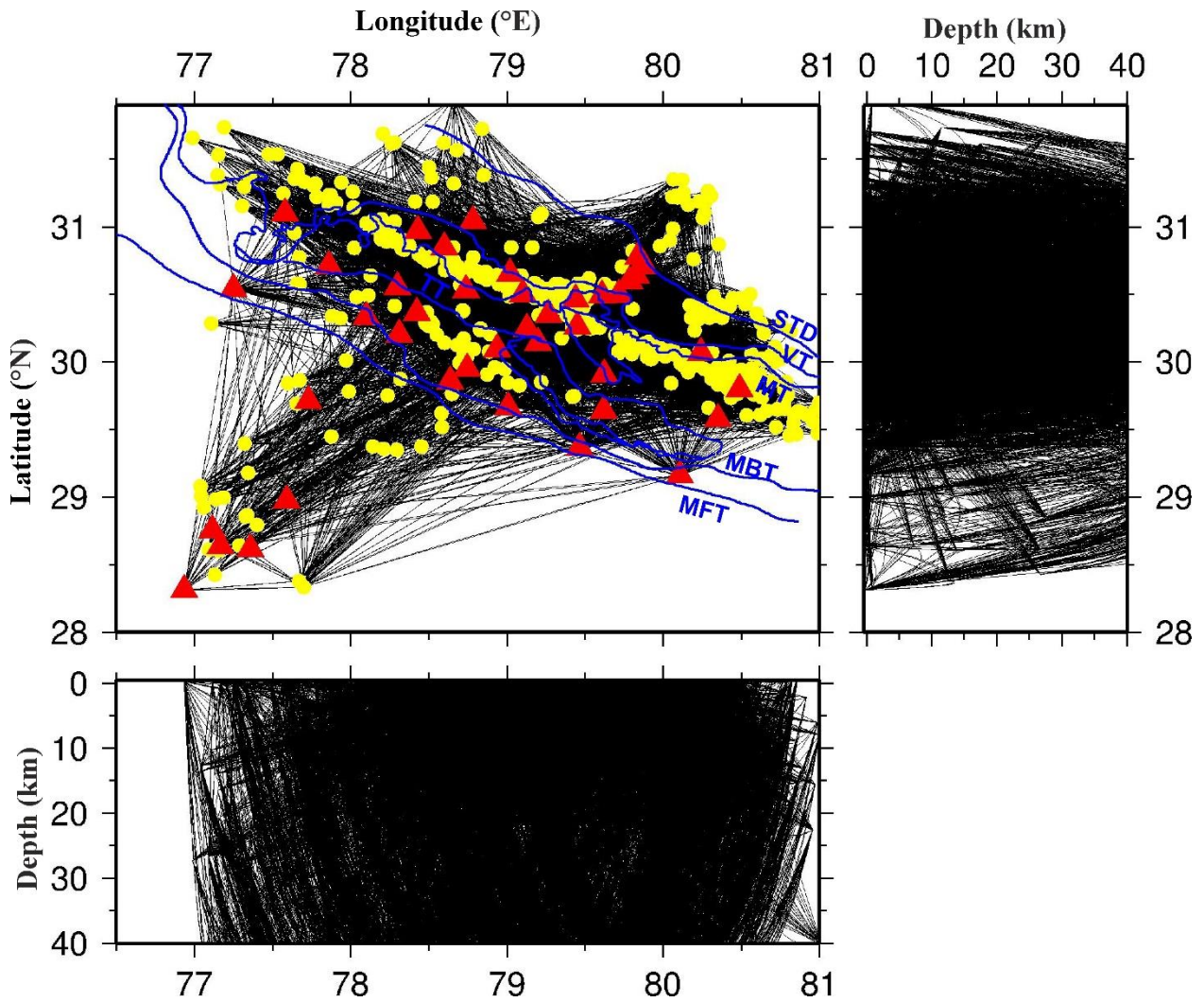


**Figure 2:** 3-D distribution of seismic ray paths. The seismic stations and events are shown by red triangles and yellow dots, respectively. Major tectonic boundaries (as shown in Fig. 1b) are also projected with blue lines.

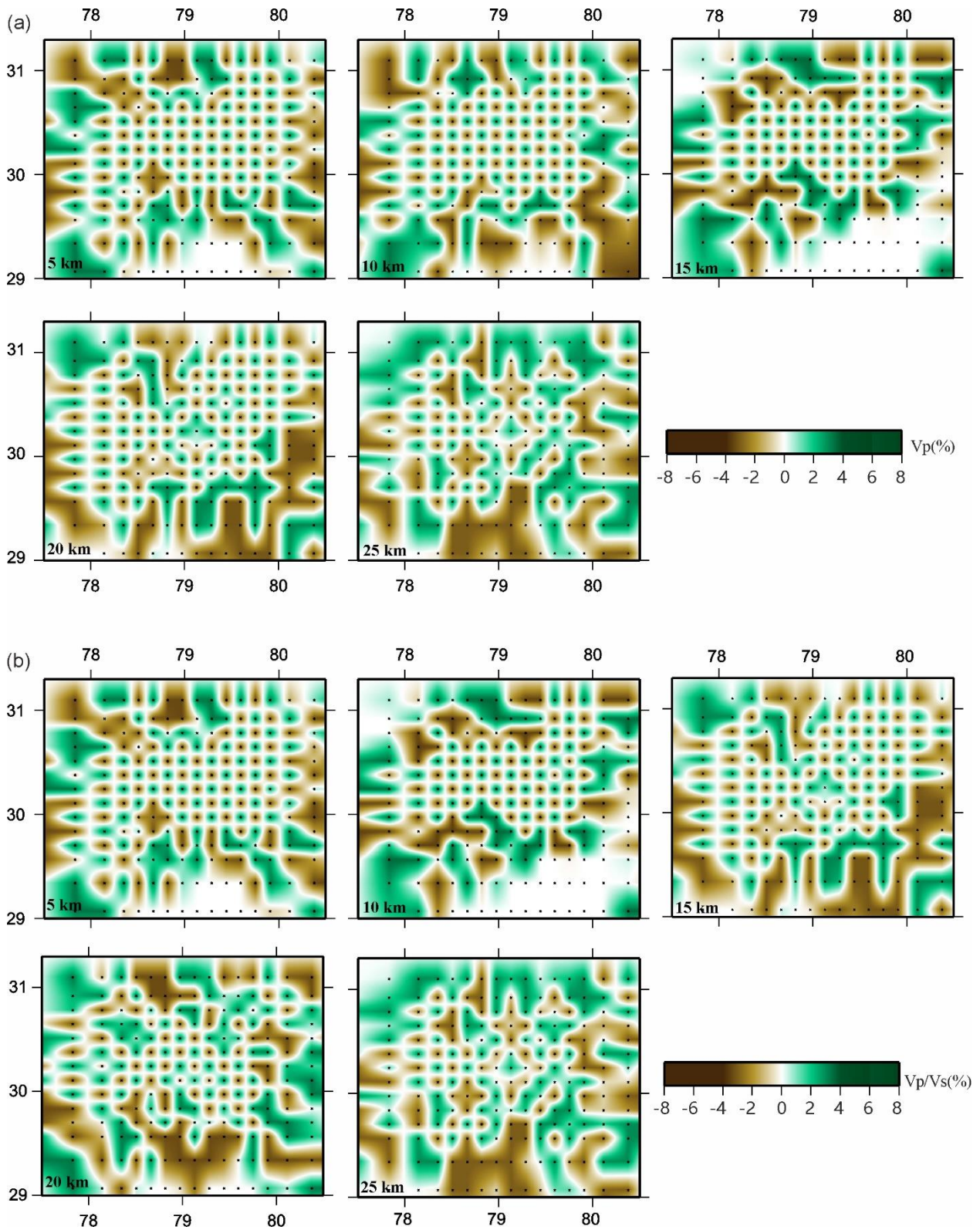


**Figure 3:** Results of the checkerboard resolution tests (CRT) for  $V_p$  (a), and  $V_p/V_s$  (b). Layer depth is shown on the lower-left corner of each map. Scales for perturbation values (in %) for both  $V_p$  and  $V_p/V_s$  are shown in the right.

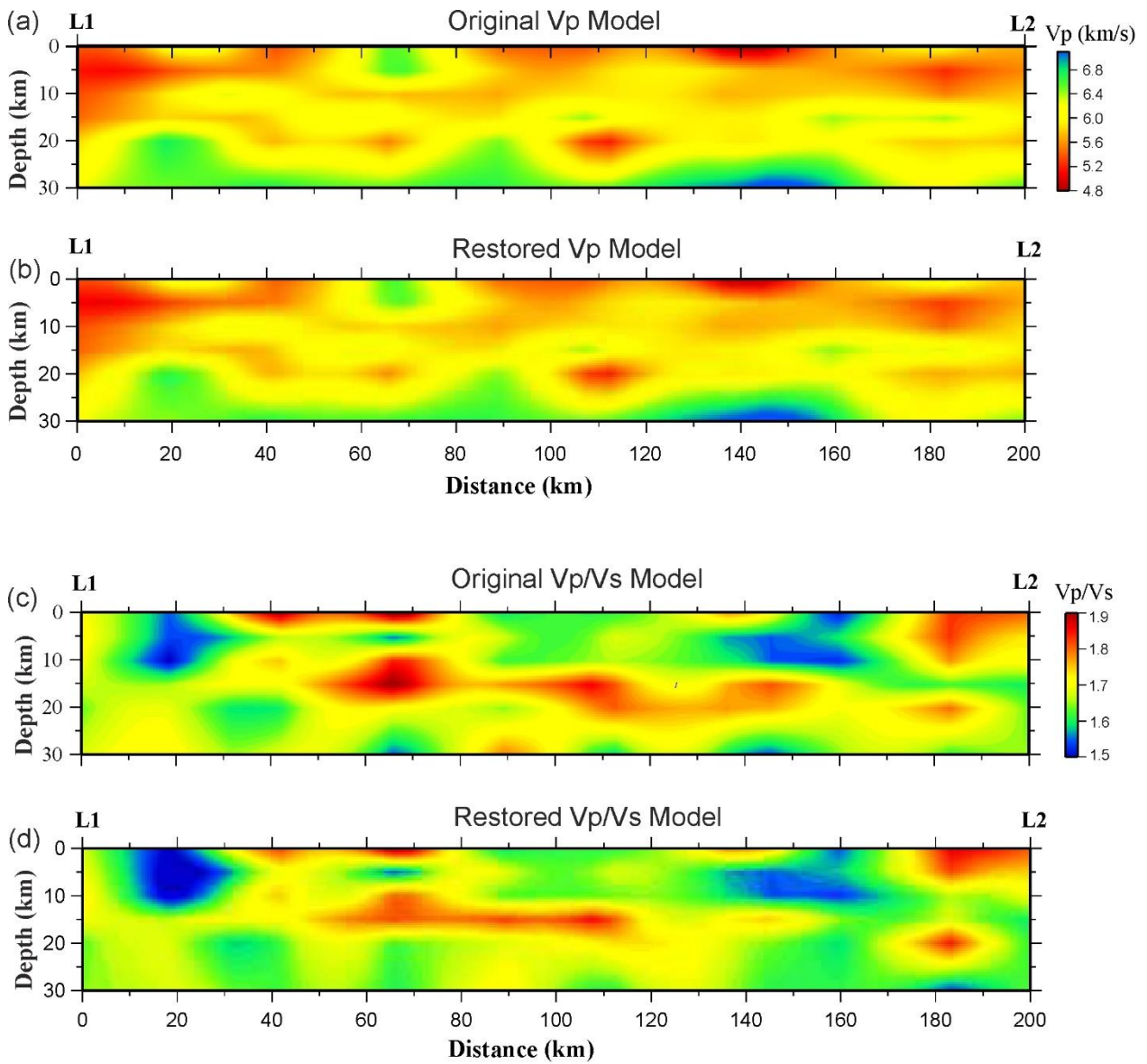


**Figure 4:** Results of restoring resolution test along a L1-L2 (as shown in Fig. 6). Panels (a) and (b) show the original and restored models for  $V_p$ , respectively. Panels (c) and (d) show the original and restored models for  $V_p/V_s$ , respectively. Kindly refer the text (section 4.1) for detail.

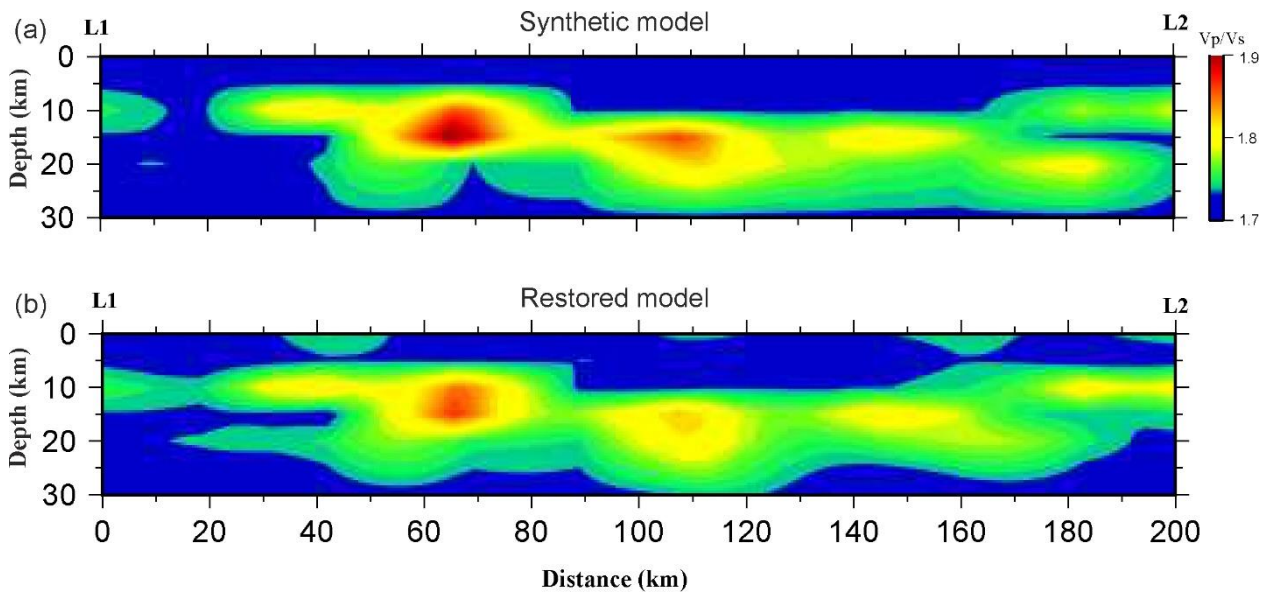


**Figure 5:** Results of synthetic test along a L1-L2 (as shown in Fig. 6). Panels (a) and (b) show the original and restored models for  $V_p/V_s$ , respectively. Kindly refer the text (section 4.1) for detail.

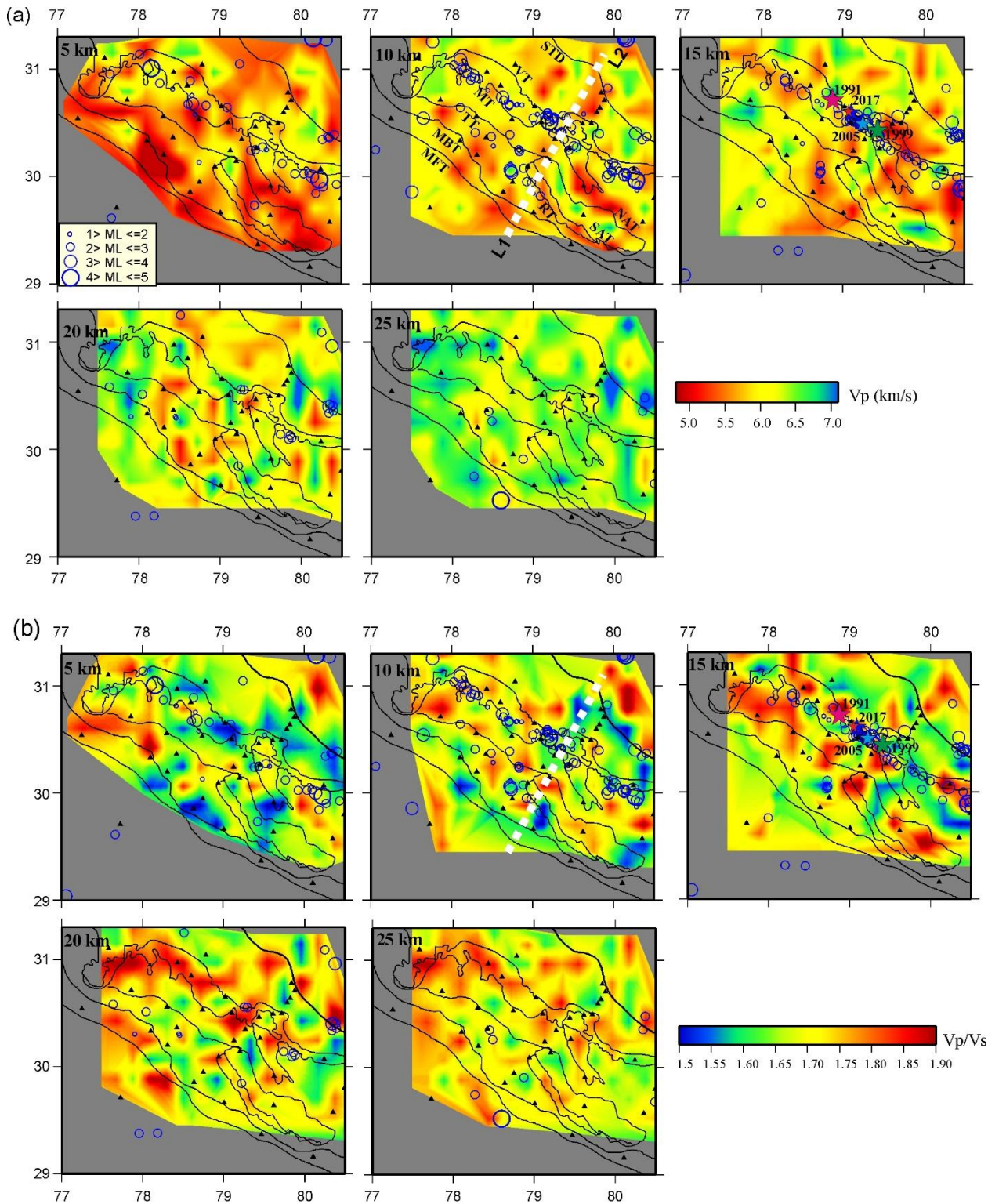


**Figure 6:** Plan view of tomographic images of absolute  $P$ -wave velocity ( $V_p$ ) (a) and  $V_p/V_s$  (b). Layer depth is shown on the upper-left corner of each map. The  $V_p$  and  $V_p/V_s$  scales are shown at the bottom of respective plots. Poorly resolved areas are masked by gray colour in each plot. Small open circles indicate the small magnitude earthquakes during 2006-2008, which occurred within 2 km of each depth slice. Earthquake magnitude scale is shown in lower-left plot of Fig. 6a. Moderate-to-strong magnitude ( $5.0 < M < 7.0$ ) earthquakes in the region are shown with different stars, same as mentioned in Fig. 1. Tectonic boundaries are same as shown in Fig. 1b. L1 - L2 shows the location of cross-section, used for showing  $V_p$  and  $V_p/V_s$  images to correlate with the MHT across the Kumaun-Garhwal Himalaya in Fig. 7.

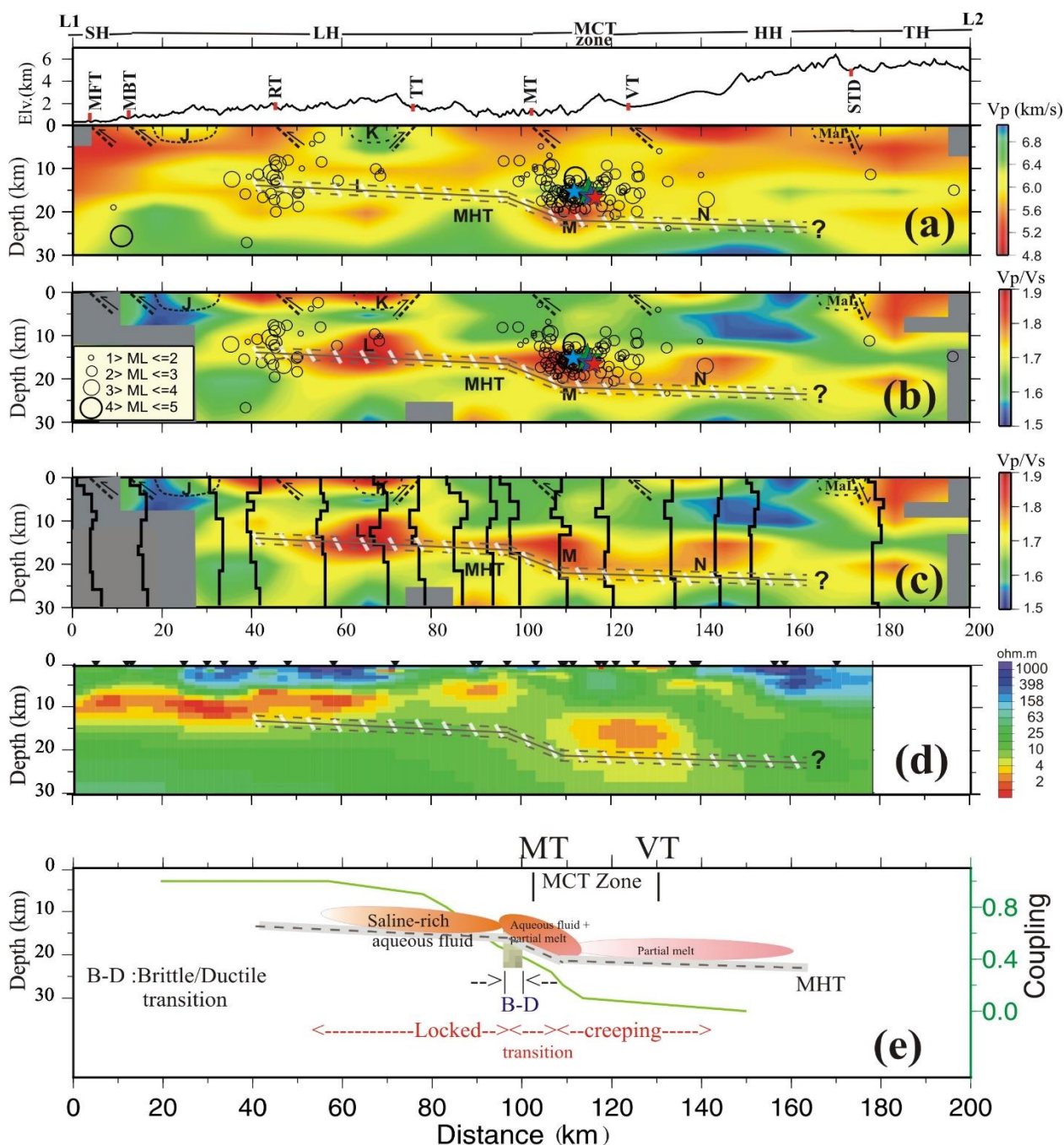


**Figure 7:** (a, b) Vertical cross-sections of the  $P$ - wave velocity ( $V_p$ ) and  $V_p/V_s$  images along the profile L1-L2 (as shown in Fig. 6). Small open circles show small magnitude earthquakes that occurred within 50 km width on either side of the profile and recorded during 2006-2008. Moderate-to-strong magnitude ( $5.0 < M < 7.0$ ) earthquakes in the region are shown with different stars, same as mentioned in Fig. 1. The inferred MHT (continuous black line) along with uncertainty (dotted line with white slanting lines) are projected over these images. MaL represents the Malari Leucogranites. Please see text for details of the inferred features (“J”, “K”, “L”, “M”, “N”, “MaL” and MHT). Topography variation along the profile is shown on the top. (c) Inferred MHT and 1-D shear wave velocity models using receiver function modelling (Kanna and Gupta, 2020) superimposed over obtained  $V_p/V_s$  images. (d) Inferred MHT superimposed over resistivity values (Rawat et al., 2014). (e) Schematic diagram showing the nature and geometry of the MHT (gray colour with dash lines) in the Garhwal Himalaya and its role in earthquake genesis, by combing observation from seismology, magnetotellurics and GPS. Green line shows the seismic coupling derived from the slip deficit rate (Yadav et al., 2018). Its scale is shown on the right axis. H/V is 1:1 for the Figs. 7 (a-d).



### Supplementary Figures

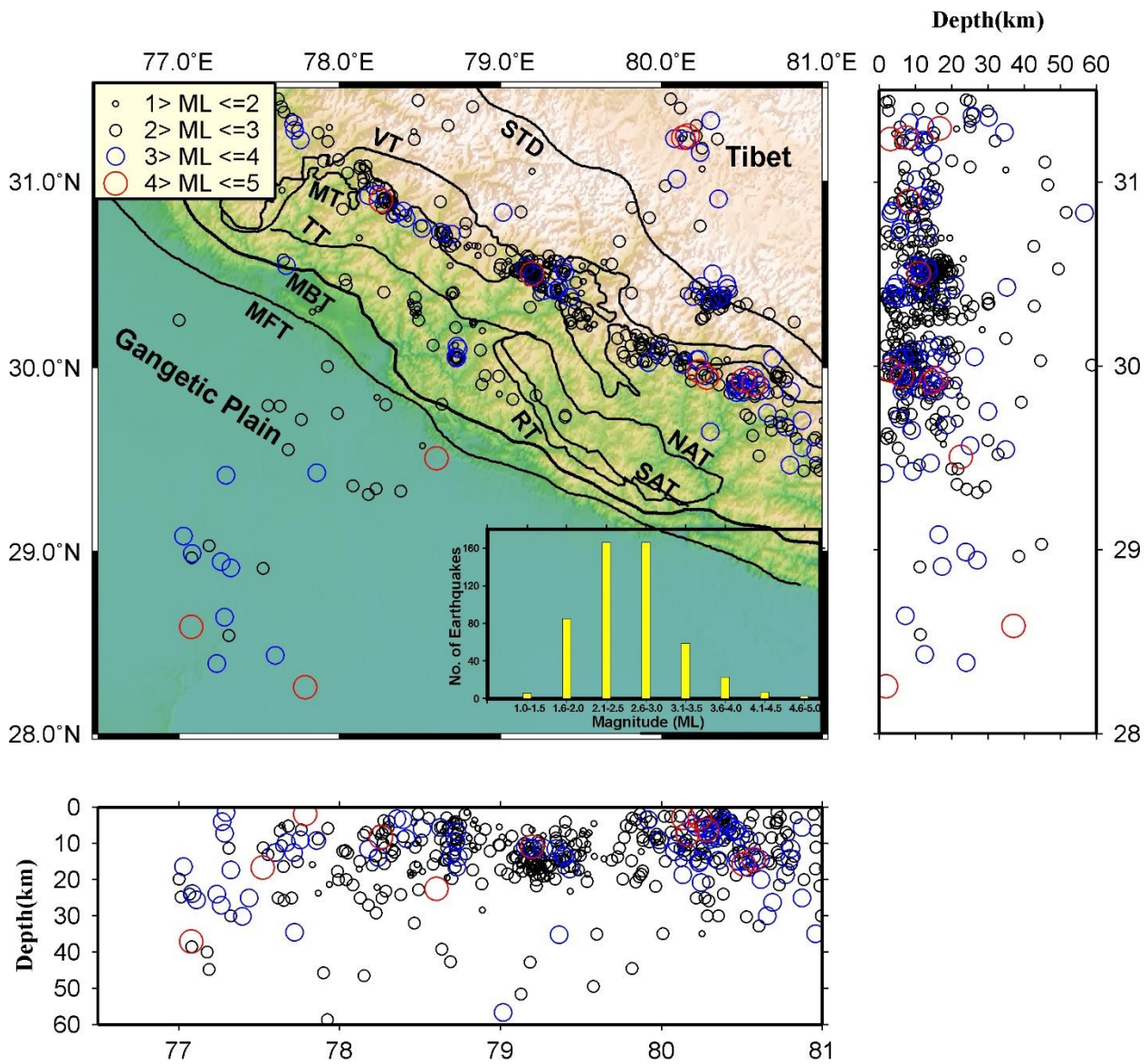


**Fig. S1:** 3-D distribution of the 515 earthquakes (open circles) used in the study. The size and colour of open circles represents the earthquake magnitude as per inset in the top-left corner of the plot. The earthquake magnitude histogram is shown in lower-right side of the plot. Depth scale is exaggerated.

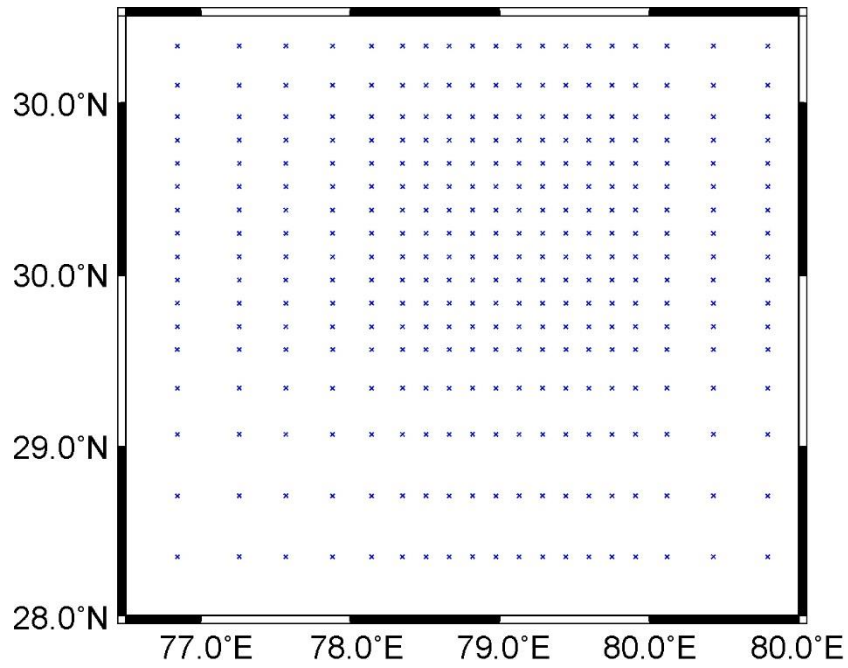


**Fig. S2:** Grid point distribution in the plan view. The same grid points were taken at different depths (5, 10, 15, 20, 25 and 55 km).

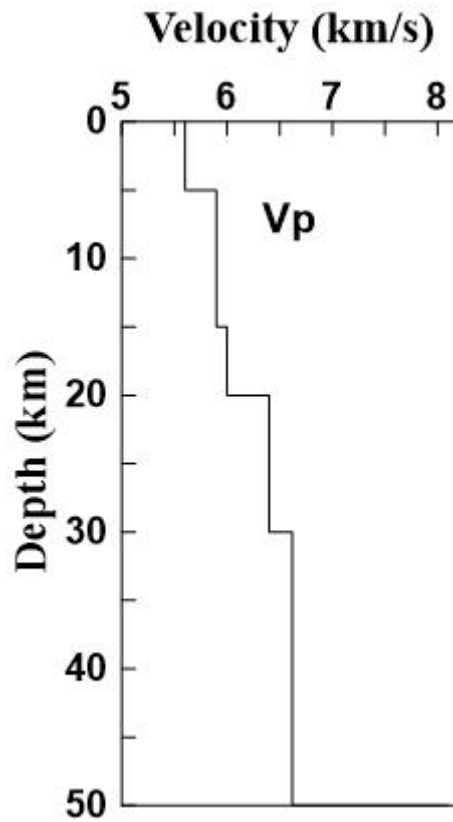


**Fig. S3:** Initial 1-D velocity model (Mahesh et al., 2013) used for the tomography.

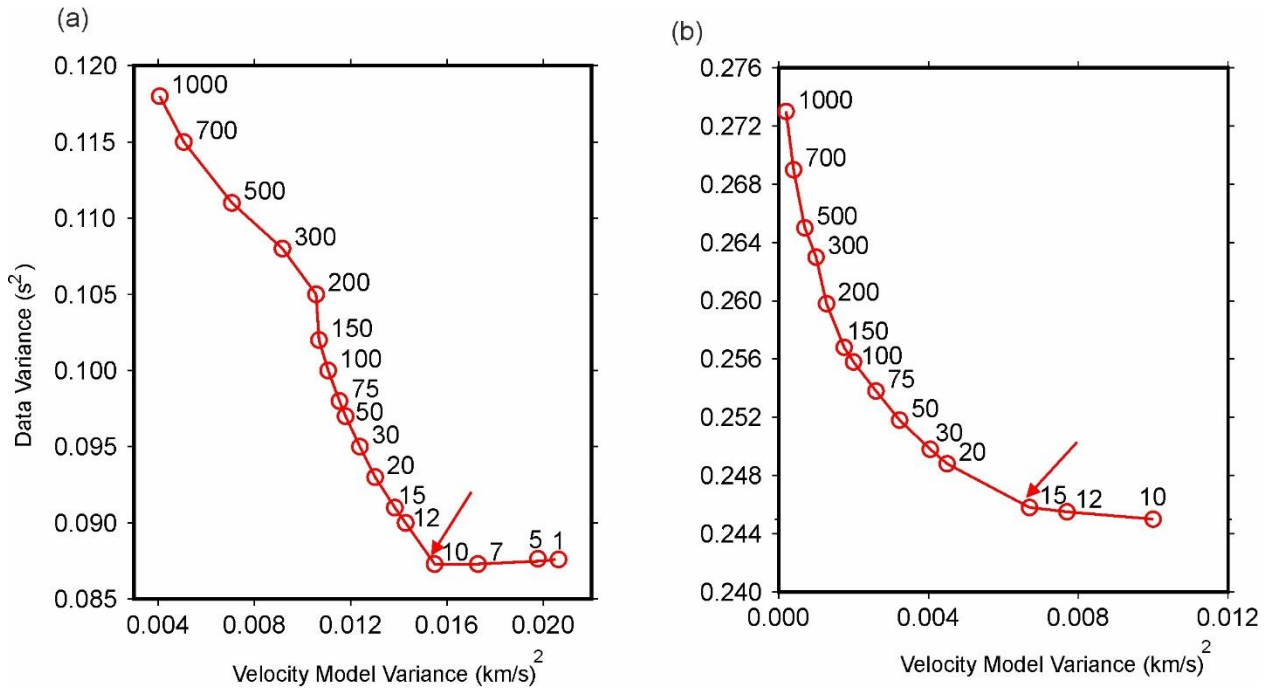


**Fig. S4:** Trade-off curves between data variance and model variance for  $V_p$  (a) and  $V_p/V_s$  (b), used to select the optimal damping parameters to obtain the optimum 3-D  $V_p$  and  $V_p/V_s$  images.

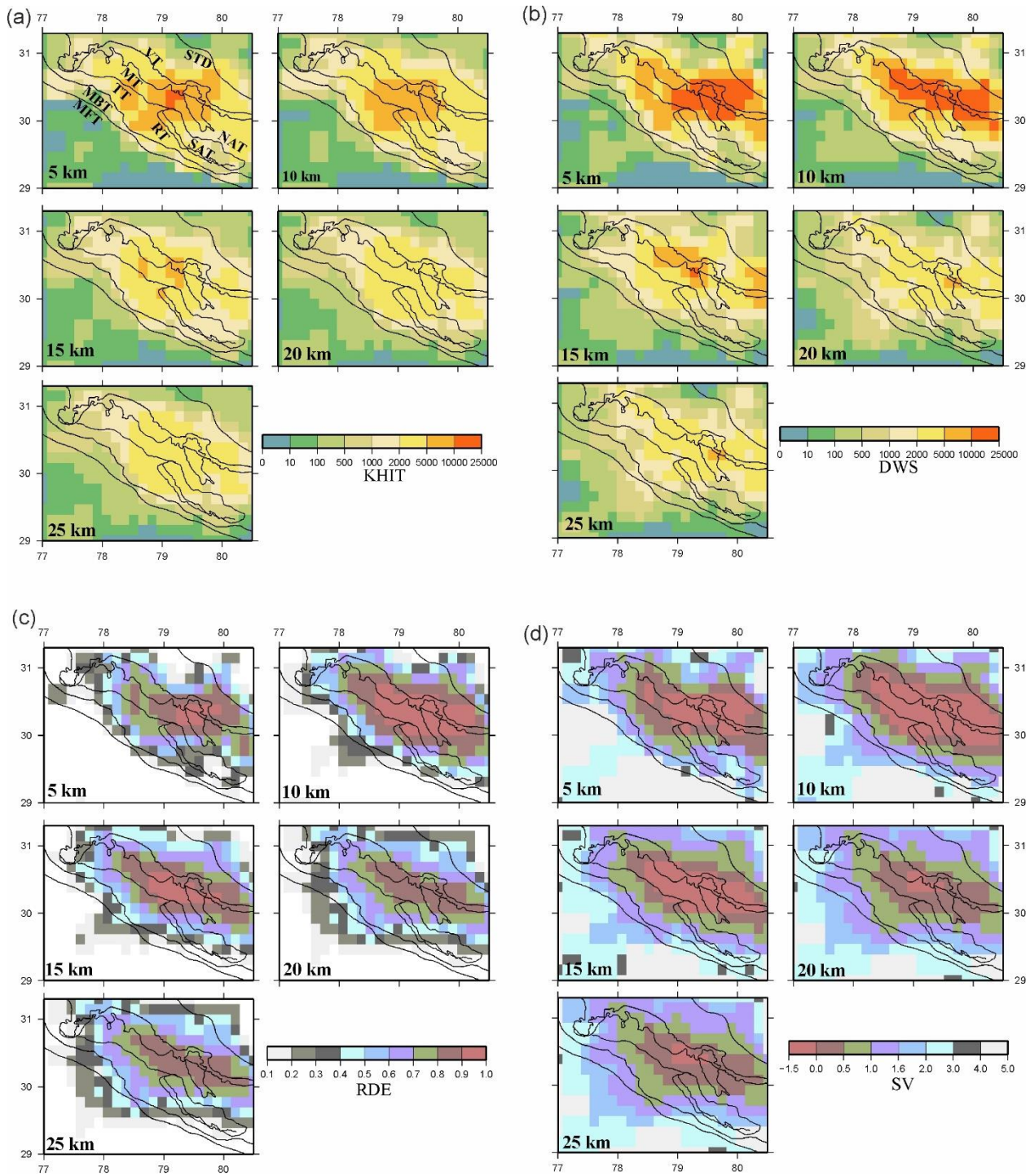


**Fig. S5:** (a) Total number of hit per cell (KHIT), (b) Derivative Weighted Sum (DWS), (c) Resolution Diagonal Element (RDE), and (d) Spread Value (SV) of resolution matrix for  $V_p$  at different depths. Layer depth is shown on the lower-left corner of each map. Tectonic boundaries are same as shown in Fig. 1.

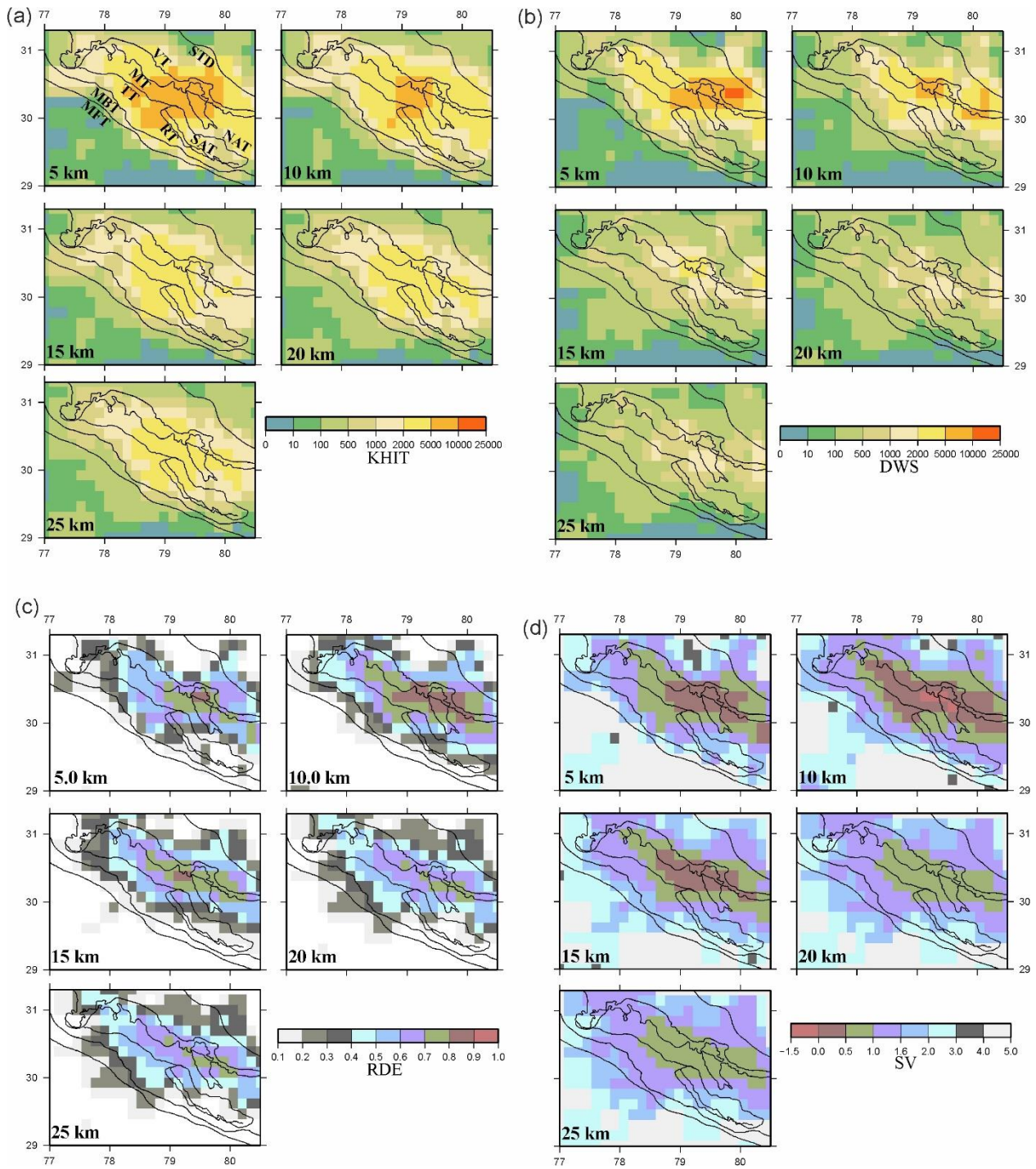


**Fig. S6:** (a) Total number of hit per cell (KHIT), (b) Derivative Weighted Sum (DWS), (c) Resolution Diagonal Element (RDE), and (d) Spread Value (SV) of resolution matrix for  $V_p/V_s$  at different depths. Layer depth is shown on the lower-left corner of each map. Tectonic boundaries are same as shown in Fig. 1.

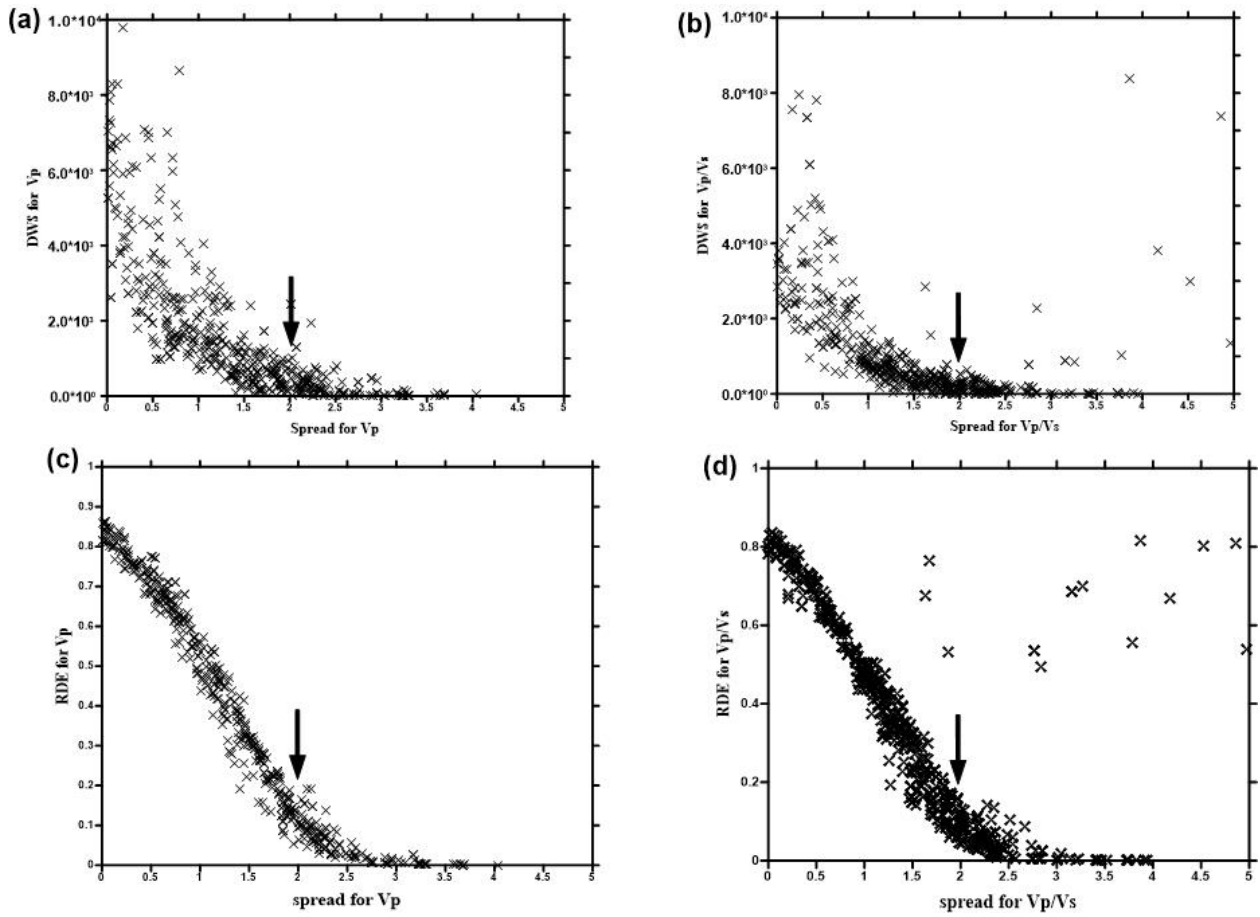


**Fig. S7:** Derivative Weighted Sum (DWS) versus Spread Values (SV) for  $V_p$  (a) and  $V_p/V_s$  (b). Resolution Diagonal Element (RDE) value versus Spread Values for  $V_p$  (c) and  $V_p/V_s$  (d). The arrows indicate the threshold values of the Spread Value chosen to delineate poorly resolved in subsequent velocity maps.

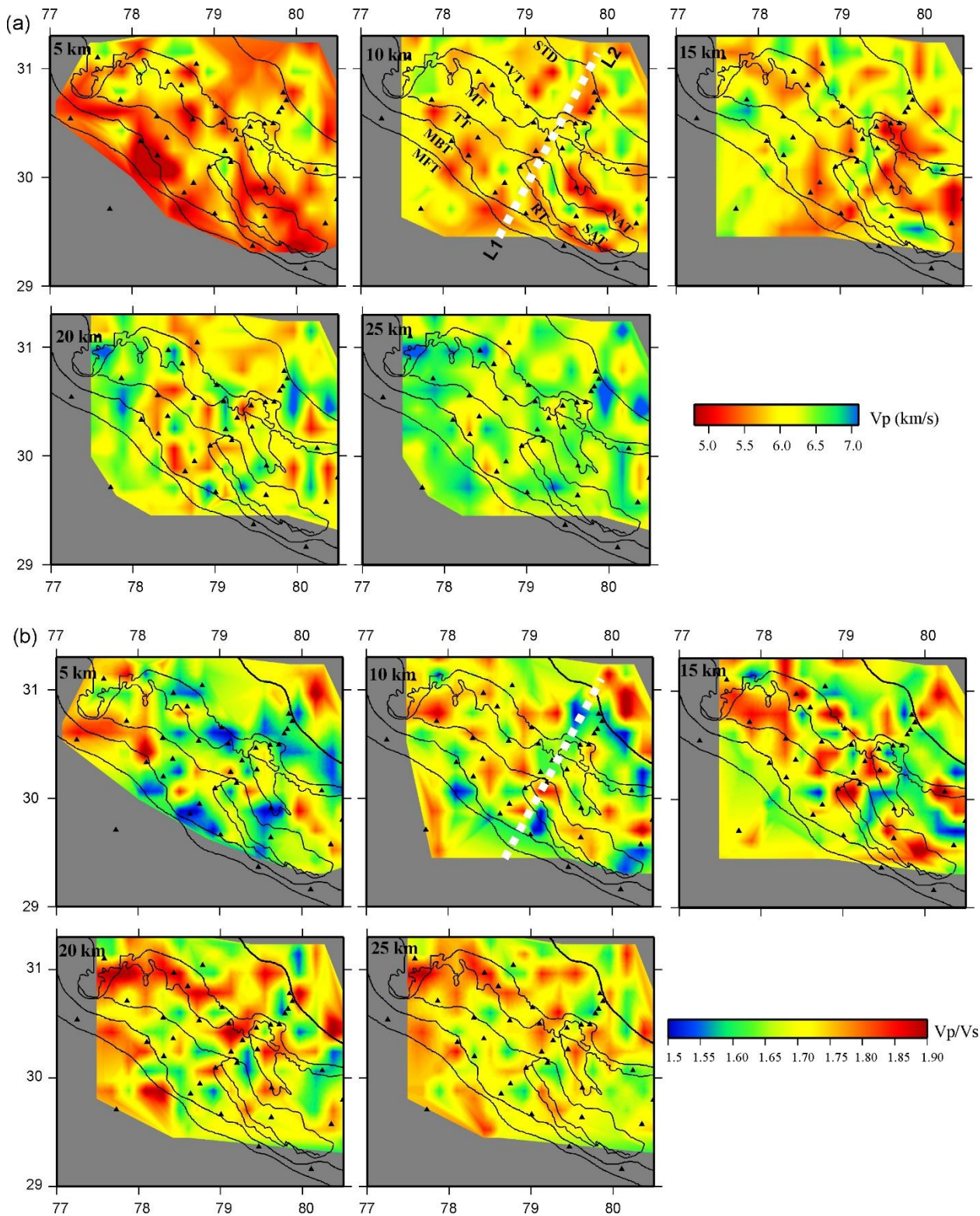


**Fig. S8:** Plan view of tomographic images of absolute  $P$ -wave velocity ( $V_p$ ) (a) and  $V_p/V_s$  (b), same as Fig. 6, however without earthquakes.

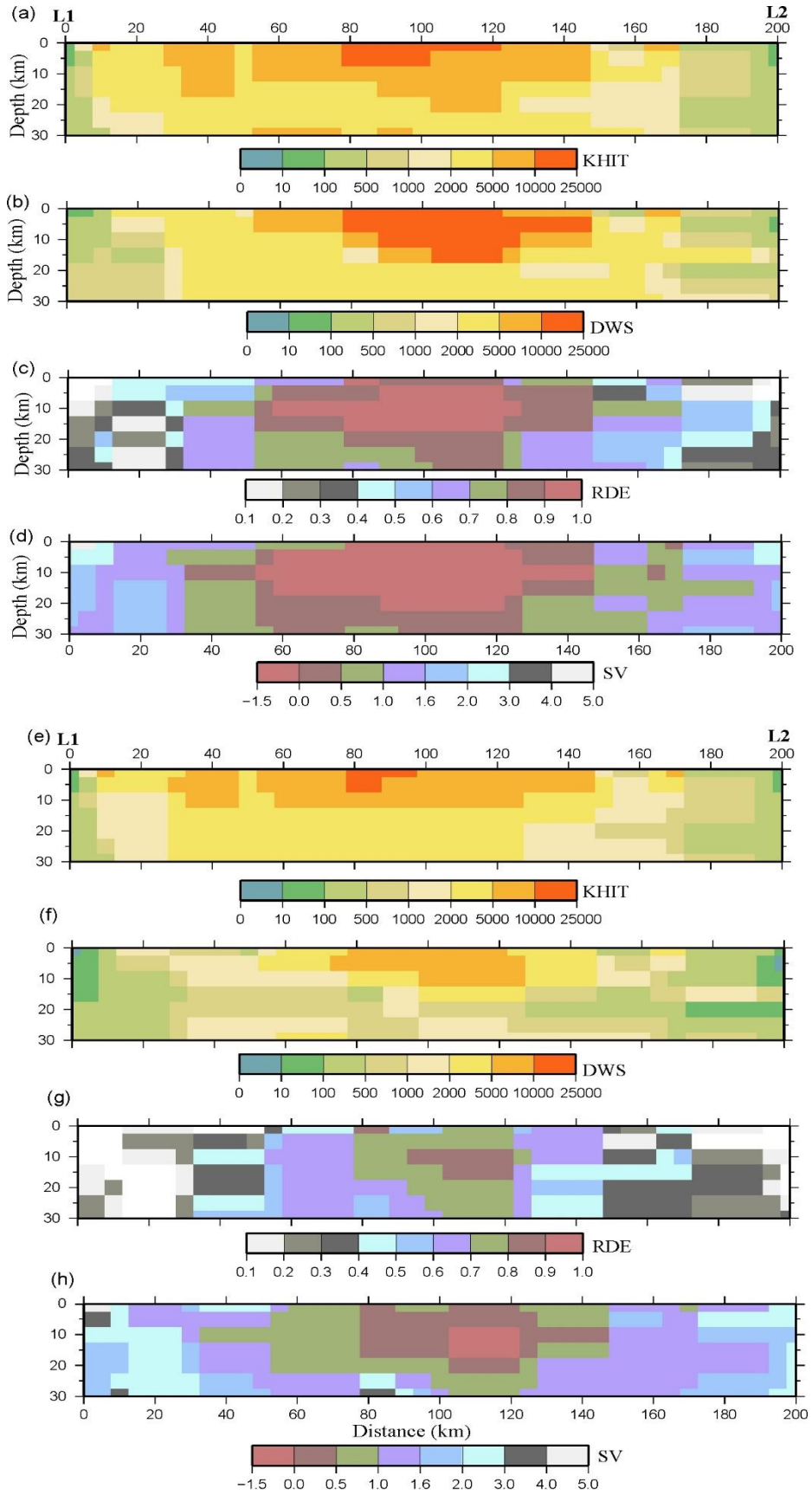


**Fig. S9:** Total number of Hit (KHIT), Derivative Weighted Sum (DWS), Resolution Diagonal Element, and Spread Value (SV) of resolution matrix for  $V_p$  (a, b, c, d) and for  $V_p/V_s$  (e, f, g, h) along the profile L1-L2 (as shown in Fig. 6).